MOLECULAR BIOLOGY

Slow RNAPII elongation enhances naive pluripotency rewiring while maintaining high replication fork speed

Sara Martín-Vírgala[1]†, Joana Segura[1]†, Alicia Gallego[1]†, Ran Tong[1], Sara Tur-Gracia[1], Jesús Rafael Rodriguez-Aguilera[1], Biswajit Das[2], Javier Isoler-Alcaraz[1], Carlos Gallego-García[1], Shraddha Shinde[3,4], Magdalena M. Maslon[3], Andrei Chabes[2], Lothar Schermelleh[5], María Gómez[1]*

DNA replication and transcription must be intricately coordinated as both machineries navigate the same chromatin landscape to ensure genome stability and proper cell function. Here, we show that altering their elongation rates—specifically, slowed transcriptional elongation alongside rapid replication fork progression—does not elicit replicative stress. Instead, this independent kinetic variation accelerates the acquisition of naive pluripotency during in vitro dedifferentiation, revealing an unexpected link between transcription kinetics and cell plasticity. Mechanistically, we show that the transition to naive pluripotency is accompanied by a distinctive alternative splicing program indicative of reduced RNA polymerase II (RNAPII) elongation. These findings redefine the functional relationship between replication and transcription dynamics and uncover transcriptional velocity as a tunable layer of control over cellular identity transitions.

INTRODUCTION

DNA replication and transcription are two essential processes that use the genome as a template. Accumulated evidence over the past decades showed that conflicts between them threaten genome stability (*1*–*4*). To minimize the potentially detrimental collisions between translocating replication and transcription complexes, cells have evolved a myriad of strategies. This includes co-orienting the directionality of both processes, most evident in bacteria (*5*), initiating replication close to transcription start sites (TSSs) of genes (*6*–*9*), using ongoing transcription to push replicative helicases away from the gene bodies (*10*–*13*), or even delaying the duplication of the TSS of active genes till very late in the cell cycle (*14*). Beyond this, recent research has revealed a tight relationship between the two processes when they co-occur in the genome, as shown by the rapid rebinding of active RNA polymerase II (RNAPII) complexes onto replicated DNA minutes after the passage of the replication fork (*15*, *16*). This coupling might facilitate a rapid reestablishment of the transcriptional program after DNA replication, thus contributing to maintaining cellular identity (*16*, *17*).

An unexplored angle of the cross-talk between the two processes concerns the speed at which they occur in the genome. In bacteria, the replication rate is around 12 times faster than the transcription rate [600 nucleotides (nt)/s versus 50 nt/s, respectively] (*18*). Thus, the divergent replication forks emanating from the single bacteria replication origin would unavoidably collide with transcribing polymerases. The fact that the large majority of highly expressed and essential genes are codirectionally oriented relative to the replisome across bacterial species limits the potentially more harmful head-on encounters (*19*, *20*). In contrast, in the large genomes of mammalian cells, where DNA replication initiates from thousands of replication origins, the speed of elongating RNAPII and replication forks falls within a similar range (17 to 33 nt/s versus 17 to 72 nt/s, respectively) (*18*). Similar translocation rates, in principle, might help minimize the encounters between both machineries. The general mechanism underlying the orientation-specific effects of replication-transcription conflicts (TRCs) is likely the generation of positive supercoils ahead of the replication and transcription complexes (*21*–*24*). Whether comparable elongation speeds contribute to limiting topological stress and thereby decreasing the frequency of TRCs is not known.

Here, we set out to investigate the relevance of balanced replication-transcription rates for genome function. For that, we used mouse embryonic stem cells (mESCs) carrying a single-residue substitution in the funnel domain of RPB1 (Arg^{749} to His; R749H), the largest subunit of RNAPII. The R749H mutation impairs early mouse development; however, R749H mESCs can be maintained in culture and exhibit a slow transcription elongation phenotype, as determined by metabolic labeling of newly transcribed RNAs with 4sU upon transcription synchronization and sequencing (4sU-seq), overall resulting in more than a 25% reduction in the average transcription rate compared to wild-type (WT) cells (*25*). By combining time-resolved analyses of transcriptome rewiring and replication dynamics upon cell dedifferentiation, we show that slow RNAPII transcription promotes naive pluripotency while maintaining fast replication fork speed. Moreover, we found that unbalanced transcription and replication rates do not generate replicative stress, suggesting that modulating RNAPII velocity could provide a means to enhance cell plasticity and reprogramming.

RESULTS

Slow transcription elongation rate facilitates fast replication fork rate and alleviates replicative stress

To investigate the impact of slow transcriptional rates on DNA replication, we used mESCs carrying an R749H RNAPII knock-in (RNAPII-mut) generated at the Cáceres laboratory (*25*). Replication elongation rates were addressed by stretched DNA fiber assays (Fig. 1A) and showed that RNAPII-mut cells display moderate but consistent faster replication forks than their WT counterparts [mean values of 1.101

[1]Centro de Biología Molecular Severo Ochoa (CBM), Consejo Superior de Investigaciones Científicas/Universidad Autónoma de Madrid (CSIC/UAM), C/ Nicolás Cabrera 1, 28049 Madrid. Spain. [2]Dept. of Medical Biochemistry and Biophysics, Umeå University, SE 901 87 Umeå, Sweden. [3]Malopolska Centre of Biotechnology, Jagiellonian University, Krakow, Poland. [4]Doctoral School of Exact and Natural Sciences, Jagiellonian University, Lojasiewicza 11, 30-348 Krakow, Poland. [5]Department of Biochemistry, University of Oxford, South Parks Road, Oxford OX1 3QU, UK.
*Corresponding author. Email: mgomez@cbm.csic.es
†These authors contributed equally to this work.

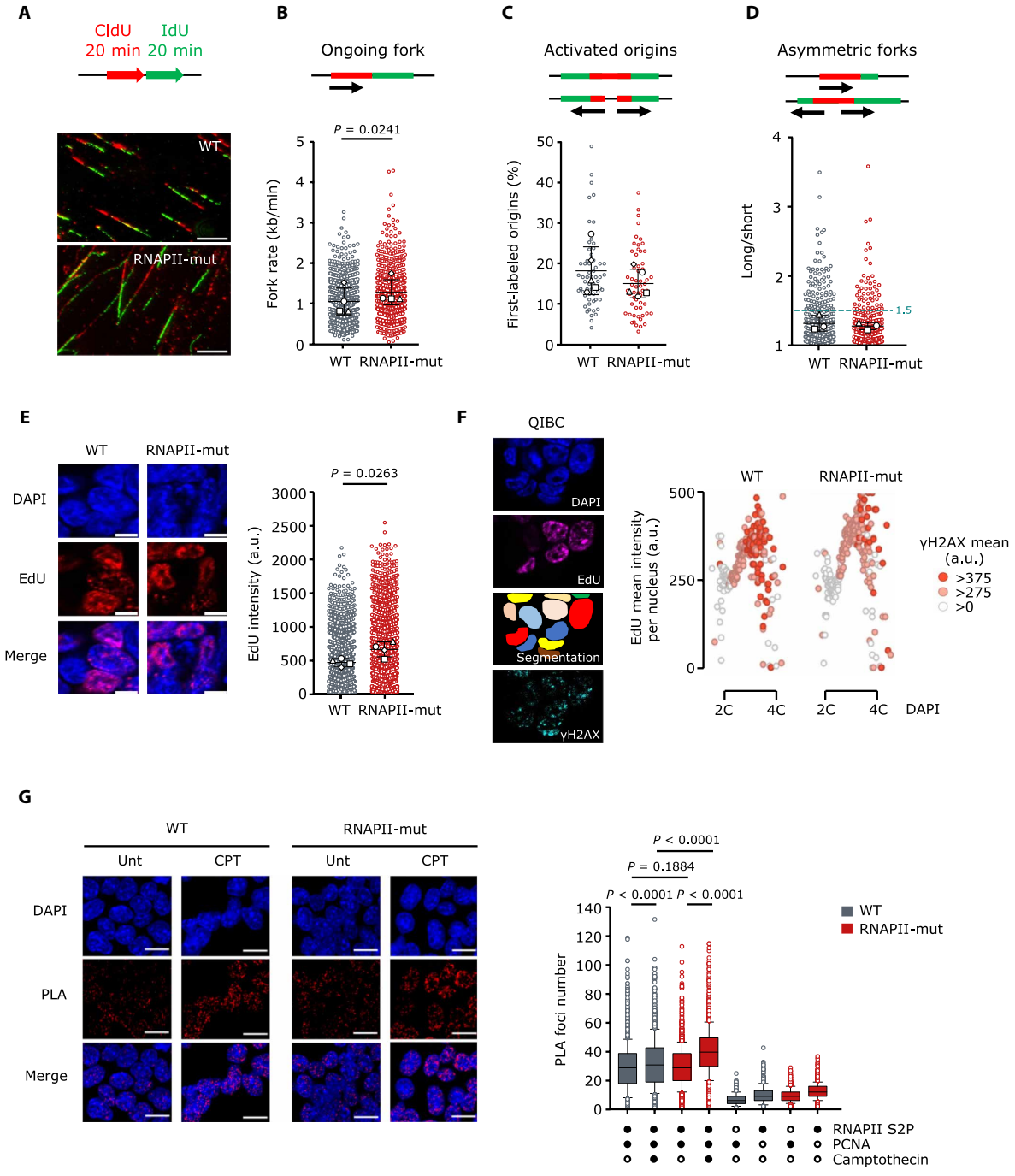

Fig. 1. Slow transcription elongation facilitates faster replication without generating replicative stress. (**A**) Experimental design and representative images of stretched DNA fibers from WT and RNAPII-mut cells. Scale bars, 10 μm. (**B** to **D**) Plots displaying the fork rate (B), first-labeled origins (FLO; C), and fork asymmetry (D) from WT and RNAPII-mut cells. Mean values for each replicate are indicated with open symbols ($n > 3$). Mean of the means is indicated by a horizontal line with SD. $n > 841$ tracks for fork rate, $n > 311$ origin structures for FLO, and $n > 339$ tracks for asymmetry measurements. The threshold for considering fork asymmetry is 1.5 [green dashed line in (D)]. (**E**) Representative confocal microscopy images and plots showing the EdU Click-iT signal in WT and RNAPII-mut cells. Cells were pulse labeled with 10 μM EdU for 20 min before fixation. Scale bars, 5 μm. a.u., arbitrary units. Mean values are as in (B) to (D) ($n = 4$). WT, $n = 2622$; RNAPII-mut, $n = 2206$. Significant paired two-tailed *t* test of means is indicated [(B) to (E)]. (**F**) QIBC scatterplots of the DNA content (DAPI) versus the EdU signal, showing the γH2AX nuclear intensity in a color scale at the different cell cycle phases. One representative experiment is shown, with $n = 18{,}000$ analyzed nuclei per condition. Nuclei displayed on the graphs were grouped into DAPI intensity intervals of 5000 units each (binning). (**G**) Representative RNAPII S2P + PCNA PLA images and quantification of PLA foci per nuclei in WT and RNAPII-mut cells at the indicated conditions. Scale bars, 15 μm. PLA foci are shown as boxplots ($n = 2$), with the center line indicating the median, boxes showing the 25th to 75th percentiles, and whiskers showing the 10th to 90th percentiles. Foci numbers outside the whiskers are shown as points. $n > 833$ analyzed nuclei per condition. The Mann-Whitney test was conducted, and significant *P* values are indicated.

and 1.326 kilobases (kb)/min for WT and RNAPII-mut cells, respectively] (Fig. 1B). This increase in fork speed, however, did not lead to a significant compensatory effect on the number of active replication origins (Fig. 1C) nor affected the symmetrical progression of the forks (Fig. 1D). Measuring global DNA synthesis rates by 5-ethynyl-2′-deoxyuridine (EdU) incorporation, either by immunofluorescence or flow cytometry, confirmed the enhanced replication of RNAPII-mut cells (Fig. 1E and fig. S1A, left). Increased replication rates did not alter the overall duration of the cell cycle nor the proportion of cells in the different substages of the S phase (fig. S1, A to C). Consistent with unperturbed DNA replication progression, RNAPII-mut cells did not show signs of DNA damage or replication stress (fig. S1D). On the contrary, slower transcription and faster replication resulted in slightly reduced levels of γH2AX signaling (fig. S1, D and E), more evident at the late S phase (Fig. 1F). This result was not due to RNAPII-mut cells having an impaired response to DNA damage because γH2AX signaling was readily increased when cells underwent replicative stress upon aphidicolin (Aph) exposure or DNA damage by γ-irradiation (fig. S1, D, F, and G). To test the extent to which slower RNAPII elongation might alleviate TRCs, we exposed cells to mild concentrations of the Topoisomerase I inhibitor camptothecin (CPT) and measured TRCs by proximity ligation assays (PLAs) between the elongating form of RNAPII phosphorylated at Ser^2 (RNAPII S2P) and PCNA, a key component of the replisome (Fig. 1G). Whereas nuclear PLA foci were comparable between cell types under untreated conditions, RNAPII-mut cells displayed significantly higher foci numbers than WT cells upon CPT treatment. We interpreted this result as a synergic effect of the drug with the fast-moving forks of RNAPII-mut cells, increasing the likelihood of collisions with CPT-trapped Topoisomerase I cleavage complexes.

Faster fork rates with a similar number of active origins should result in a shorter S-phase length. To determine whether this was the case, cells were synchronized at the G_1-S border by a double thymidine (Thy) block, and DNA synthesis along the S phase was monitored by flow cytometry (fig. S2A). RNAPII-mut cells enter early-S more rapidly and progress faster to late-S (fig. S2, A and B), resulting in a slightly shorter S phase. To address whether the Thy block affects replication dynamics differently in each cell type, we performed DNA fiber analyses at 1, 3.5, and 6 hours after Thy release, representing early, mid, and late S-phase time points (fig. S2C). We found that the fork rate accelerates along the S phase in both cell types, in agreement with a recent work using scEdU sequencing in HeLa cells (*26*). To note, faster fork speed was less apparent in RNAPII-mut synchronized cells, suggesting that the prolonged G_1 arrest might partially suppress the faster fork phenotype. In line with this interpretation, Thy-arrested RNAPII-mut cells display elevated Chk1P levels relative to asynchronous cells (fig. S2D). Despite some differences at the late-S time point, the overall fork dynamics along the S phase were comparable between WT and RNAPII-mut cells.

Replication-transcription encounters remain similar despite differences in transcription and elongation rates

PLA results suggest a similar number of encounters between the replication and transcription machineries regardless of alterations in their relative speeds (Fig. 1G, untreated cells). Because the equivalent R749H mutation in *Drosophila* (R741H) shows a diminished ability to read through intrinsic elongation blocks (*27*), which might alter its processivity on chromatin, we next quantified the number of active transcriptional complexes in the S phase using super-resolution three-dimensional (3D) structured illumination microscopy (3D-SIM). This approach provides improved volumetric resolution and enhanced contrast compared to conventional fluorescence microscopy and has recently been used to resolve individual cohesin and soronin molecules in human cells (*28*). By 3D-SIM, most of the RNAPII S2P resolved spots are likely single molecules because the vast majority displayed homogeneous intensity and size (Fig. 2A and fig. S2E): an ovoid of ~120 nm in diameter (3 pixels), full width at half maximum in *xy*, and 300 nm in the *z* direction. RNAPII S2P foci quantification (fig. S2E) and chromatin fractionation experiments (fig. S2D) showed that both WT and RNAPII-mut cells have a similar number of elongating transcriptional complexes in the early and mid S phase. We then exploited the high definition of 3D-SIM to measure the colocalization of RNAPII S2P with sites of ongoing replication. To maximize the resolution of our analyses, cells were labeled with EdU for a brief 5-min pulse (labeling nascent DNA fragments of around 5 kb in euchromatic replication) (Fig. 2A). We found that the percentage of overlapping EdU/RNAPII S2P foci per nucleus decreased from the early to mid S phase (Fig. 2B) but was comparable between cell types at both sub-S phases. Notably, the average overlap between elongating replication and transcription sites per nucleus matches previous estimations in human cell lines (*16*). We speculate that the reduced cell-to-cell variation in the colocalization frequency of replication and transcription sites in early S-phase RNAPII-mut cells could result from their more homogeneous and slower transcription elongation rates (*25*).

To determine whether the R749H mutation leads to altered levels of active RNAPII complexes on nascent DNA, cells were labeled with EdU for 5 min followed by increasing chase times to assess RNAPII S2P occupancy after replication (Fig. 2C). We observed significant increases in the percentage of overlapping EdU/RNAPII S2P foci from 20-min chase time, reaching their maximum at 40 min (Fig. 2D). These results are consistent with a previous work reporting increased levels or residence time of RNAPII S2P on nascent DNA up to 40 min after replication fork passage (*16*). As before, no significant differences were found between WT and RNAPII-mut cells, indicating that the dynamics of RNAPII onto replicated DNA were similar in both cell types. Thus, slow transcription and faster replication do not alter the frequency of encounters between both machineries nor the occupancy of active RNAPII complexes on replicated DNA.

RNAPII-mut cells reach a fully naive pluripotency state without reducing replication fork rates

mESCs in culture fluctuate between multiple interconvertible states, and this metastability and plasticity are thought to underlie their pluripotent identity (*29*–*32*). To understand the functional implications of slow transcription elongation on cell plasticity, we challenged WT and RNAPII-mut mESCs to undergo in vitro dedifferentiation by adding a two-inhibitor cocktail (2i) containing MEK and GSK3 inhibitors to the culture medium. This well-established 7-day protocol insulates cells from differentiation stimuli, shifting the population toward a more undifferentiated state known as naive pluripotency (*33*, *34*). For simplicity, we refer to the cells at day 0 (d0) as primed [cells grown in serum and leukemia inhibitory factor (LIF); primed pluripotency state] and to the cells at d7 as naive (cells grown in serum and LIF and 2i; naive pluripotency state) (Fig. 3A). After 7 days of 2i exposure, both WT and RNAPII-mut cell colonies acquire a rounder morphology and increase the expression of the pluripotency factor NANOG while reducing the expression of the DNA methyltransferase

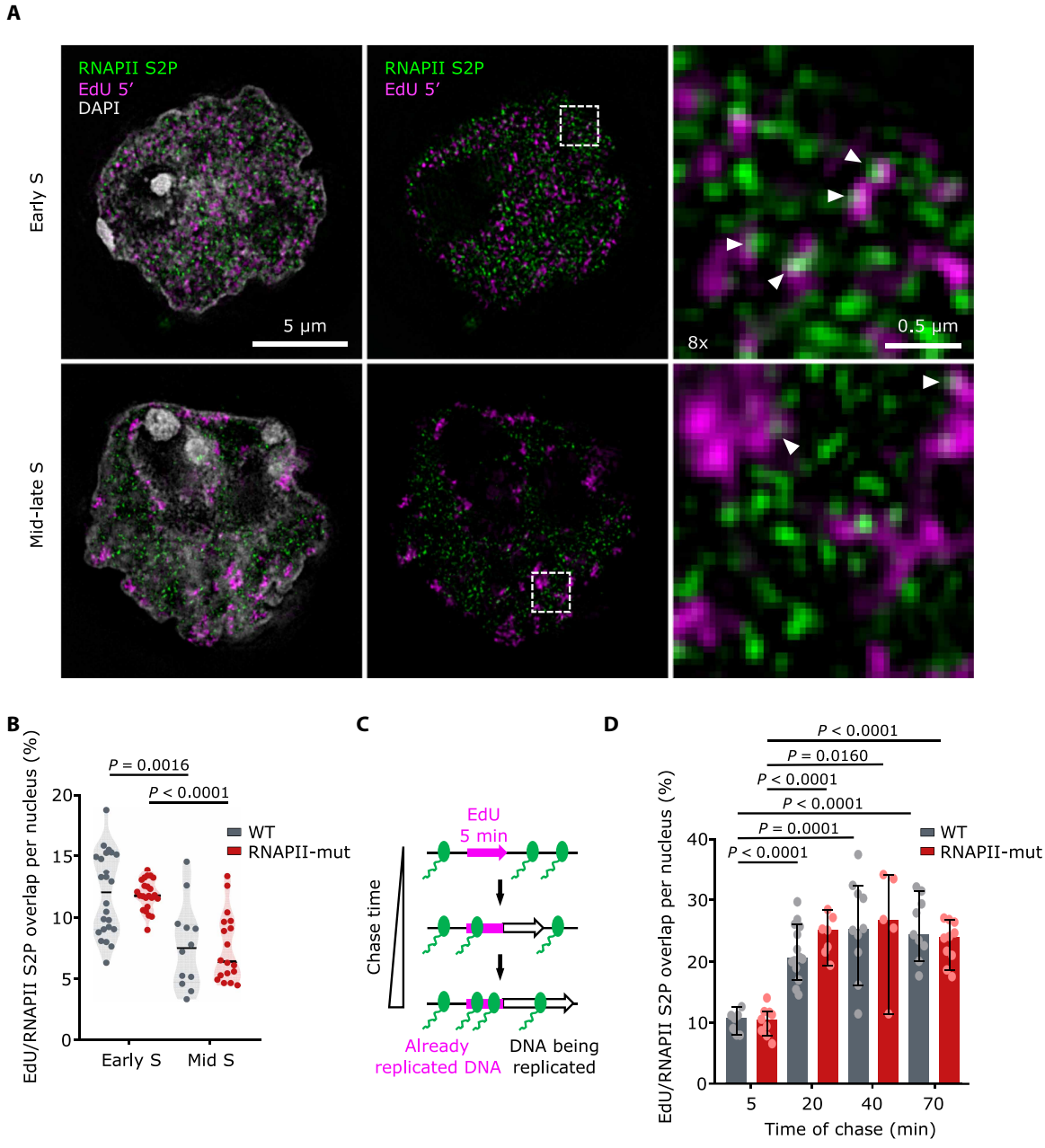

Fig. 2. The number of encounters between active replication and transcription complexes is similar in WT and RNAPII-mut cells. (**A**) Representative super-resolution 3D-SIM images of a single *xy* plane of WT cells in the early and mid S phase according to their EdU patterns, together with the RNAPII S2P foci location. Scale bar, 5 µm. Right: Zoomed image illustrating the overlapping RNAPII S2P/EdU foci (white arrowheads) quantified in (B) and (D). Scale bar, 0.5 µm. (**B**) Violin plots showing the percentage of RNAPII S2P foci overlapping with EdU per nucleus, normalized by the total number of RNAPII S2P foci in each nucleus. Median values are indicated by a horizontal line. Data are pooled from two independent experiments. Mann-Whitney test significant *P* values are shown on top. Number of nuclei: WT early, *n* = 24; RNAPII-mut early, *n* = 23; WT mid, *n* = 12; RNAPII-mut mid, *n* = 18. (**C**) Schematics of the pulse-chase experimental design to assess RNAPII S2P reloading on postreplicative chromatin in the early S phase. (**D**) Graph showing the percentage of RNAPII S2P foci overlapping with EdU per nucleus, normalized by the total number of RNAPII S2P foci in each nucleus at each chase time point. Medians and 95% confidence interval (CI) are shown. The data shown are from a single representative experiment. Number of nuclei: WT chase 5 min = 7, RNAPII-mut chase 5 min = 9, WT chase 20 min = 14, RNAPII-mut chase 20 min = 7, WT chase 40 min = 10, RNAPII-mut chase 40 min = 5, WT chase 70 min = 9, and RNAPII-mut chase 70 min = 10. Welch's test was used to assess statistical significance between groups. Significant *P* values are indicated.

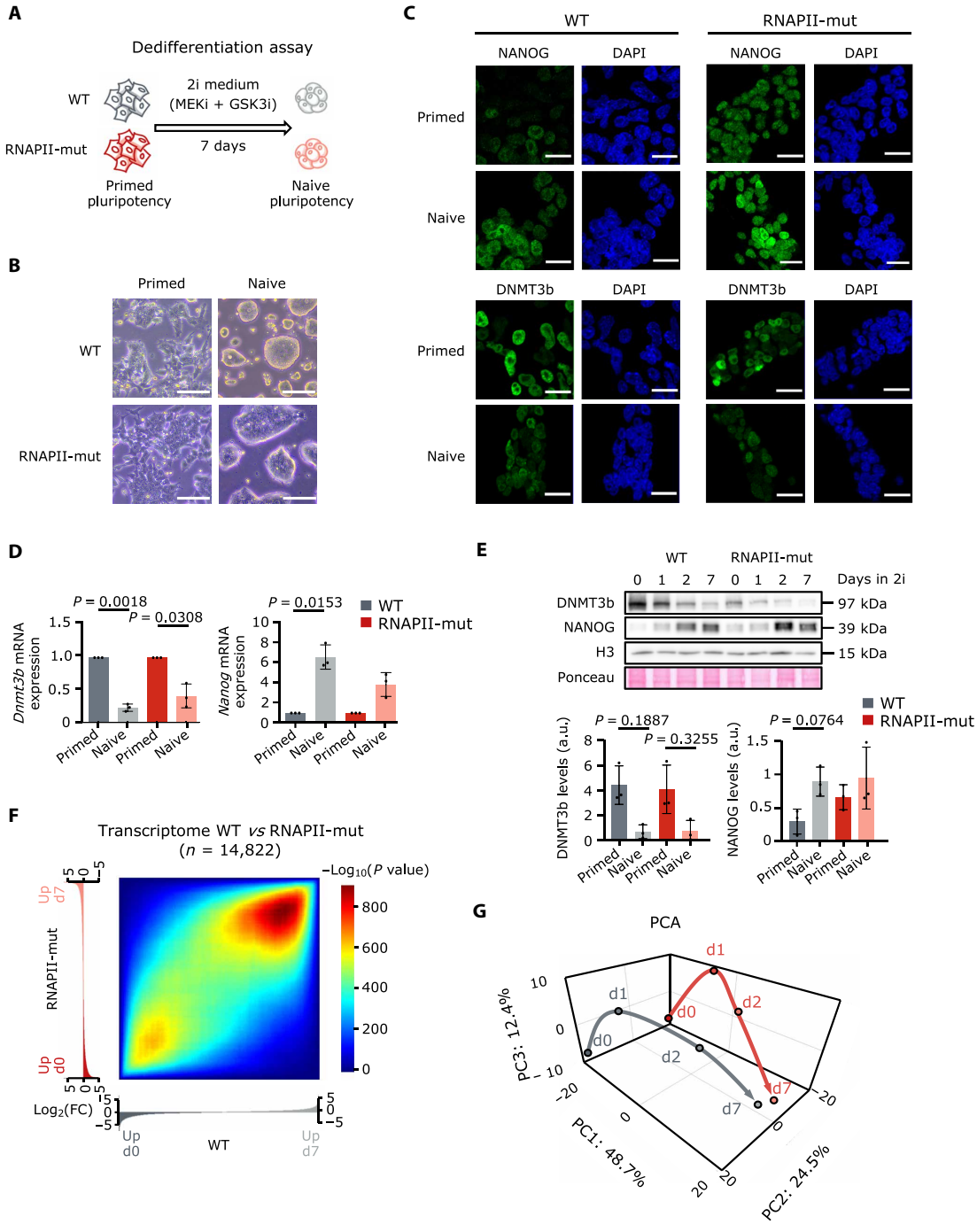

Fig. 3. RNAPII-mut cells reach a fully naive pluripotency state. (**A**) Scheme of the primed-to-naive pluripotency dedifferentiation assay. (**B** and **C**) Representative images showing the morphological changes of the colonies (B) and NANOG and DNMT3b expression on individual cells (C) after 7 days of 2i exposure for WT and RNAPII-mut cells. Scale bars, 100 μm (for bright-field images) and 15 μm (for immunofluorescence). (**D**) Histograms showing the mRNA levels of *Nanog* and *Dnmt3b* under each condition, normalized to the expression levels at the primed state. The average and SD of three independent experiments are shown ($n = 3$). Dots represent the values of individual replicates. Statistical significance was assessed by Welch's *t* test. Significant *P* values are indicated. (**E**) Top: Representative immunoblot of whole-cell extracts showing NANOG and DNMT3b levels during the indicated days of the dedifferentiation regime. Histone H3 levels and Ponceau staining were used as loading controls. The size of the detected proteins is indicated on the right. Bottom: Histograms showing NANOG and DNMT3b levels from three independent experiments ($n = 3$) for WT and RNAPII-mut cells in primed (d0) and naive (d7) states. Statistical significance was assessed by a paired two-tailed *t* test. Significant *P* values are indicated. (**F**) RRHO plot showing the significance of the overlaps between ranked sets of DEGs (d7 versus d0) in WT and RNAPII-mut cells (two biological replicates; $n = 14{,}822$ genes). First, genes were arranged by their $\log_2$[fold change (FC)] and then assessed for overlap by a RRHO sliding window of 100 genes. Color intensity represents $-\log_{10}$(*P* value) after Benjamini-Yekutieli correction of the hypergeometric overlap. (**G**) PCA based on gene expression in WT (gray) and RNAPII-mut (red) cells grown for 0, 1, 2, and 7 days in 2i medium. Dots represent the merge of two replicates under each condition. The first three principal components are shown.

DNMT3b, both at mRNA and at protein levels (Fig. 3, B to E), as reported previously (*35*–*37*). Of note, RNAPII-mut cells in the primed state displayed more homogeneous and higher levels of NANOG than their WT counterparts (Fig. 3, C and E). To evaluate whether RNAPII-mut cells fully attain the naive pluripotency identity, we performed RNA sequencing (RNA-seq) to profile gene expression along the dedifferentiation regime (d0, d1, d2, and d7 of 2i addition). Comparison of expression changes between primed and naive states in WT cells showed a significant overlap in identity and biological functions of genes that were up-regulated or down-regulated in published datasets using the same dedifferentiation regime (fig. S3A) (*35*, *37*). Differential expression analyses between RNAPII-mut and WT cell types at the primed pluripotency state (d0) identified 306 up-regulated and 393 down-regulated differentially expressed genes (DEGs) (fig. S3B). Notably, down-regulated genes exhibit greater fold change values than up-regulated genes, which may be related to the slow elongation rate phenotype of these cells. Consistent with this interpretation, down-regulated genes are significantly longer in size than the average (fig. S3C), in line with the reported down-regulation of long synaptic genes in RNAPII-mut neuronal progenitors (*25*). This was expected because longer genes tend to be more prone to RNAPII failure during elongation. In addition, down-regulated genes show low expression even in WT cells (fig. S3D), suggesting that lowly transcribed genes may be more sensitive to the R749H mutation. Whereas down-regulated DEGs account for genes related to cell migration and extracellular matrix organization, the up-regulated ones are enriched in terms related to translation (fig. S3E). Despite these differences in gene expression between WT and RNAPII-mut cells at the primed pluripotency state, the magnitude of expression changes along the dedifferentiation process was strongly correlated between cell types (Fig. 3F). In agreement, both cell types displayed parallel expression patterns of key pluripotency genes (fig. S3F). Moreover, principal components analysis (PCA) indicates that, although through different trajectories, WT and RNAPII-mut cells reach a similar naive pluripotency stage by d7 (Fig. 3G). These results imply that altering transcription and replication elongation rates does not impair mESC plasticity.

We next addressed replication fork rates in naive cells. Previous studies have shown that the 2i dedifferentiation course induces replication fork slowdown in mESCs (*35*), resembling the situation in totipotent-like cells (*38*) and in preimplantation embryos, where the speed of the forks is very slow at the initial stages and increases along development (*38*, *39*). Unexpectedly, whereas WT cells recapitulate fork slowdown during the primed-to-naive transition, RNAPII-mut cells remained fast replicating (Fig. 4A). A similar result was obtained by measuring global DNA synthesis rates by EdU incorporation (Fig. 4B and fig. S4A). To gain mechanistic insight into this phenotype, we measured the intracellular pool of ribonucleotide and deoxynucleotide triphosphates (rNTPs and dNTPs, respectively) in both cell types and cellular states. Whereas the overall rNTP levels were comparable between the four cell scenarios (fig. S4B), the dNTP/NTP ratio was significant, although only modestly higher at the naive state in both cell types (Fig. 4C), indicating that dNTP levels vary during dedifferentiation. These findings imply that fork rate slowdown (as occurs in WT naive cells) or the lack of slowdown (as occurs in RNAPII-mutant naive cells) is not linked to changes in dNTP availability.

To ensure that RNAPII-mut cells maintain reduced transcription elongation rates during dedifferentiation, we next performed time-course measurements of transcription elongation by transient inhibition of initiating RNAPIIs with 5,6-dichlorobenzimidazole 1-β-D-ribofuranoside (DRB) (Fig. 4D). In the presence of DRB, newly initiated RNAPII cannot progress to the elongation phase; however, upon DRB removal, all initiated polymerases are released and the appearance of distinct intron-exon junctions on nascent transcripts can be monitored by reverse transcription quantitative polymerase chain reaction (RT-qPCR) in a time-dependent manner (*40*). We measured how transcription proceeded through the *Itpr1* and *Utrn* genes, previously used to study the effect of the R749H mutation on RNAPII elongation dynamics (*25*). In both genes, pre-mRNA levels start to be detectable from later time points in RNAPII-mut cells (dashed lines) than in WT cells (solid lines), with the delay becoming more pronounced over greater distances (Fig. 4E). At *Itpr1*, the first 133 kb were transcribed at ~2.22 kb/min in WT cells and ~1.77 kb/min in RNAPII-mut cells, whereas downstream regions showed delayed or absent detection in the mutant. At *Utrn*, early elongation was similar in primed cells but slower in naive RNAPII-mut cells, and across the long exon 2 to 50 interval (174 kb), elongation was reduced to ~1.45 to 1.66 kb/min compared with ~2.32 kb/min in WT. These data reveal a robust, distance-dependent decrease in elongation speed imposed by the R749H mutation. Together, these results demonstrate that replication and transcription rates can vary independently without compromising genome integrity and function.

Changes in transcript isoforms suggest reduced transcription elongation speeds during earlier stages of cellular and embryonic pluripotency

Optimal transcription elongation rates are required to ensure proper alternative splicing (AS), a key process that enhances RNA diversity contributing to protein isoform variation (*25*, *41*–*47*). Changes in AS, in turn, can influence the outcome and fate of transcripts, constituting an additional layer of regulation of cellular states (*48*). We therefore set out to determine the AS profiles in naive and primed pluripotency stages and use them to infer changes in RNAPII speed at this early cell transition window.

First, we compared the total number of AS events in primed WT and RNAPII-mut cells using vast-tools, which assigned a PSI (percent spliced-in) value to each specific event (Fig. 5A and fig. S5A). As expected, we found a transcript-wide increase in the number of AS events in slow-elongating RNAPII cells, in particular higher numbers of spliced introns (Fig. 5B). This pattern was similarly observed at the original dataset characterizing the slow transcriptional speed of the R749H mutation, although the cells were grown in a different medium [2i and LIF, no serum; (*25*)] (Fig. 5C). We then computed the number of differential splicing events (ΔPSI) between the two cell types and identified 427 differentially regulated introns. Of those, RNAPII-mut cells displayed higher levels of intron retention than WT cells, a feature also observed in the other dataset (Fig. 5D and fig. S5B). Therefore, we defined the AS signature associated with slow transcription elongation in this cellular stage as a gain in intron retention events. It is important to note that only a limited subset of genes can be reliably interrogated for both transcription elongation rates (*25*) and AS, which precluded a comprehensive analysis of the relationship between gene-specific elongation rate and splicing changes.

We next quantified the ΔPSI between naive and primed pluripotency states in WT cells. This analysis identified a tendency toward increasing exon inclusion and intron retention events in naive samples (Fig. 5E and fig. S5, C and D), indicative of a distinct regulation of AS in different pluripotency stages. This trend was confirmed in

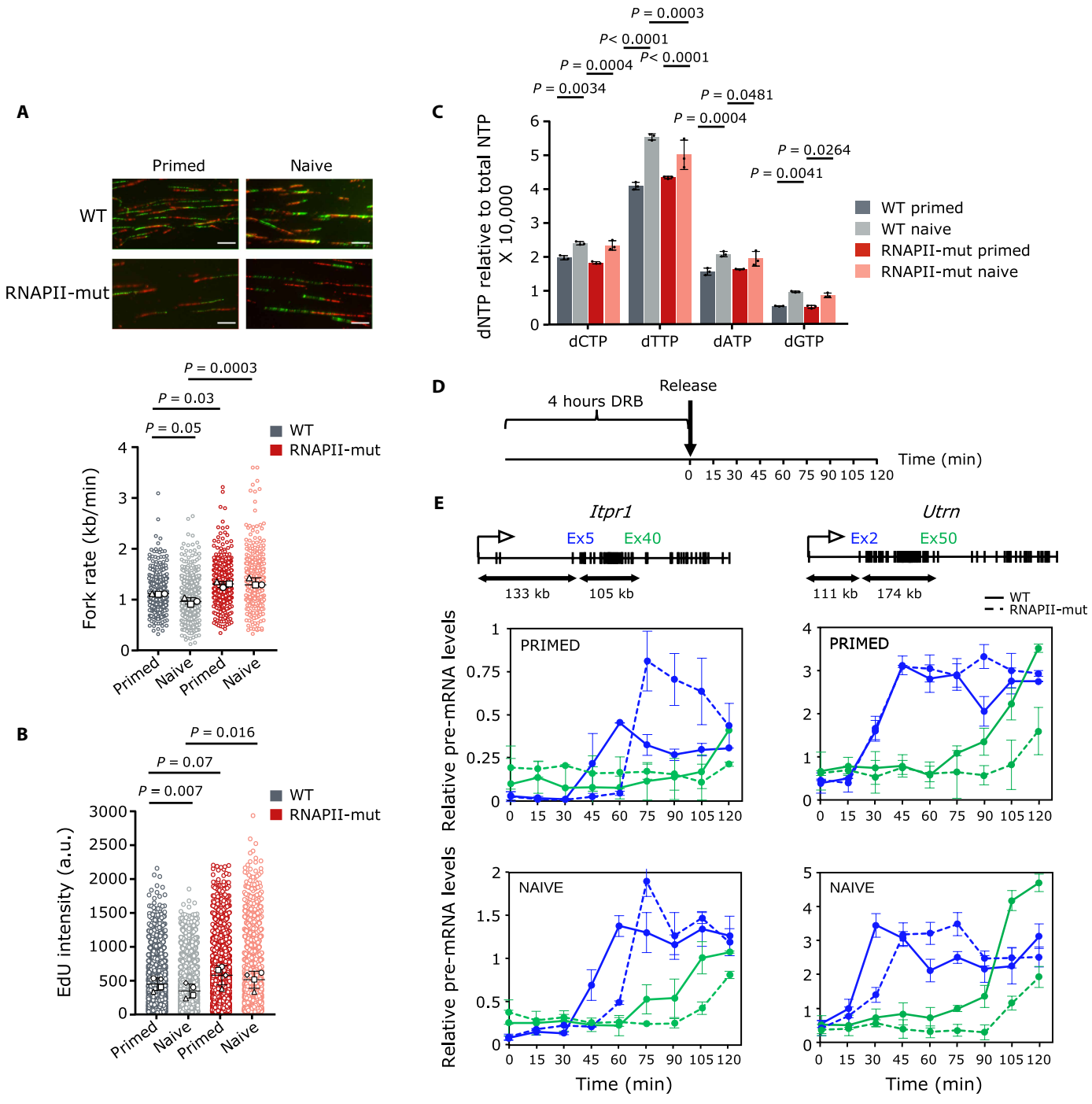

Fig. 4. RNAPII-mut cells maintain fast replication fork rates at the naive stage. (**A**) Representative images of stretched DNA fibers (top) and plots (bottom) showing fork rate measurements in primed pluripotency and naive pluripotency WT and RNAPII-mut cells. Scale bars, 10 μm. Symbols indicate mean values of the individual replicates ($n = 3$), and their corresponding mean is shown in the horizontal line and SD. $n > 386$ tracks per condition. Paired two-tailed *t* test significant *P* values are shown. (**B**) Quantification of the EdU Click-iT signal intensity per nucleus in primed and naive WT and RNAPII-mut cells. Data are from four independent experiments ($n = 4$). Symbols are as in Fig. 1E. Number of nuclei: WT primed = 3208, WT naive = 4160, RNAPII-mut primed = 3678, and RNAPII-mut naive = 3064. A paired two-tailed *t* test was conducted, and significant *P* values are indicated. (**C**) Bar graphs showing dNTP/NTP pools in primed pluripotency and naive pluripotency WT and RNAPII-mut cells. Bars show means ± SEM ($n = 3$ biological replicates). Two-way analysis of variance (ANOVA) was used to evaluate statistical significance. (**D**) Diagram of the experimental design to measure transcription elongation rates by transient inhibition of initiating RNAPIIs with DRB. (**E**) Time-course transcription elongation measurements at the *Itpr1* and *Utrn* genes in WT (solid lines) and RNAPII-mut cells (dashed lines) in primed (top) and naive (bottom) states. Levels of pre-mRNA at the indicated times were determined by RT-qPCR at the positions marked in the gene maps above the graphs. Pre-mRNA values were normalized to the values of the non-DRB–treated sample. Results are shown as means ± SD from two independent dedifferentiation replicates ($n = 2$).

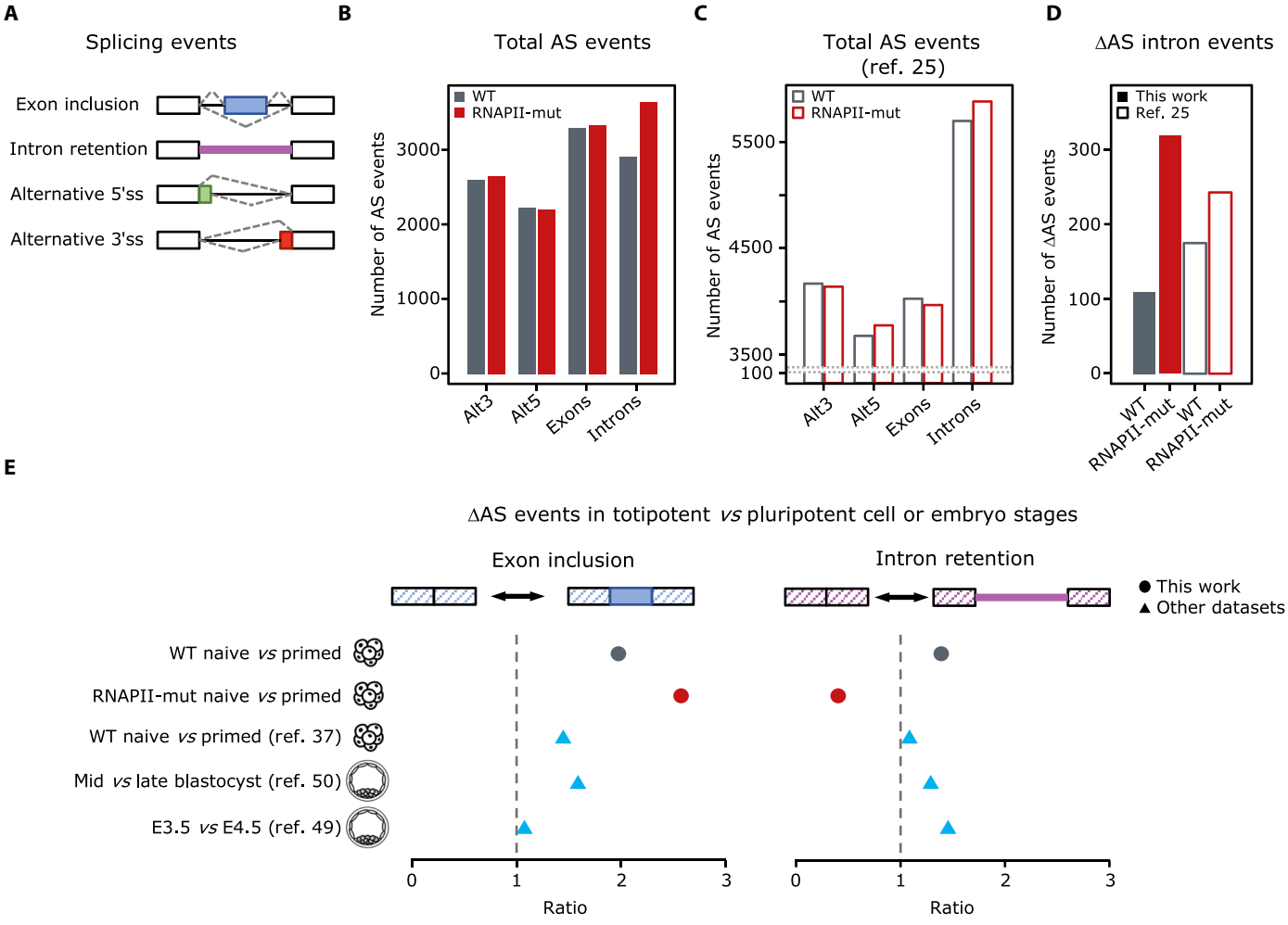

Fig. 5. Changes in transcript structure at naive and primed pluripotency cells and embryonic stages. (**A**) Schematic representation of the AS events (PSI values between 10 and 90%) analyzed. (**B** and **C**) Total number of AS events detected in merged replicates of WT and RNAPII-mut cells at the primed state (B) and in the (*25*) dataset (C), where cells were grown in no serum and LIF and 2i. (**D**) Number of differentially retained introns in RNAPII-mut versus WT in our dataset (full bars) and the (*25*) dataset (empty bars). (**E**) Differences in exon inclusion (left) and intron retention (right) levels between totipotent and pluripotent cells and embryonic stages in the indicated datasets. Data from (*37*) correspond to WT mESCs grown under similar conditions to our work (serum and LIF and 2i). Data from (*50*) and (*49*) correspond to in vivo samples from the indicated mouse embryo developmental stages. Values on the right side of the dashed line indicate higher exon inclusion or intron retention in the more totipotent stages.

datasets from a published mESC dedifferentiation course (*37*) and in datasets from mouse embryos spanning a comparable developmental period [embryonic day 3.5 (E3.5) versus E4.5 or mid versus late blastocyst, respectively] (*49*, *50*). Notably, although RNAPII-mut cells similarly display increased ratios of exon inclusion in naive versus primed pluripotency stages (Fig. 5E, left plot), they show the opposite tendency for intron retention (Fig. 5E, right plot). Because RNAPII-mut cells already displayed intron retention gains in the primed pluripotency state, this result suggests that RNAPII elongation rate is slower at naive pluripotency than at primed pluripotency in WT cells and embryos.

Slow transcription elongation accelerates the transcriptional switch toward naive pluripotency

The above results postulate that a slow transcription elongation rate could be a trait of early pluripotency stages. This hypothesis aligns with the observations that (i) RNAPII-mut cells expressed higher levels of the pluripotency marker NANOG at the primed state (Fig. 3, C and E) and that (ii) they appear more advanced toward the stabilization of the naive pluripotency state upon dedifferentiation (Fig. 3G). To unveil the molecular basis underlying this effect, we generated gene regulatory modules [Uniform Manifold Approximation and Projections (UMAPs)] based on normalized expression values (*z*-scores) of the DEGs in at least one comparison along the WT cells dedifferentiation scheme ($n = 1878$) (Fig. 6A). Genes clustered in four groups reflecting their expression trajectories across the time course: gradual or rapid decreases (clusters 1 and 2, respectively) and rapid or gradual increases (clusters 3 and 4, respectively) (Fig. 6B and fig. S6A). According to previous characterizations of the 2i-induced primed-to-naive transition, Gene Ontology (GO) enrichment analyses of these clusters revealed the silencing of genes related to multicellular organism development, cell differentiation and adhesion, and

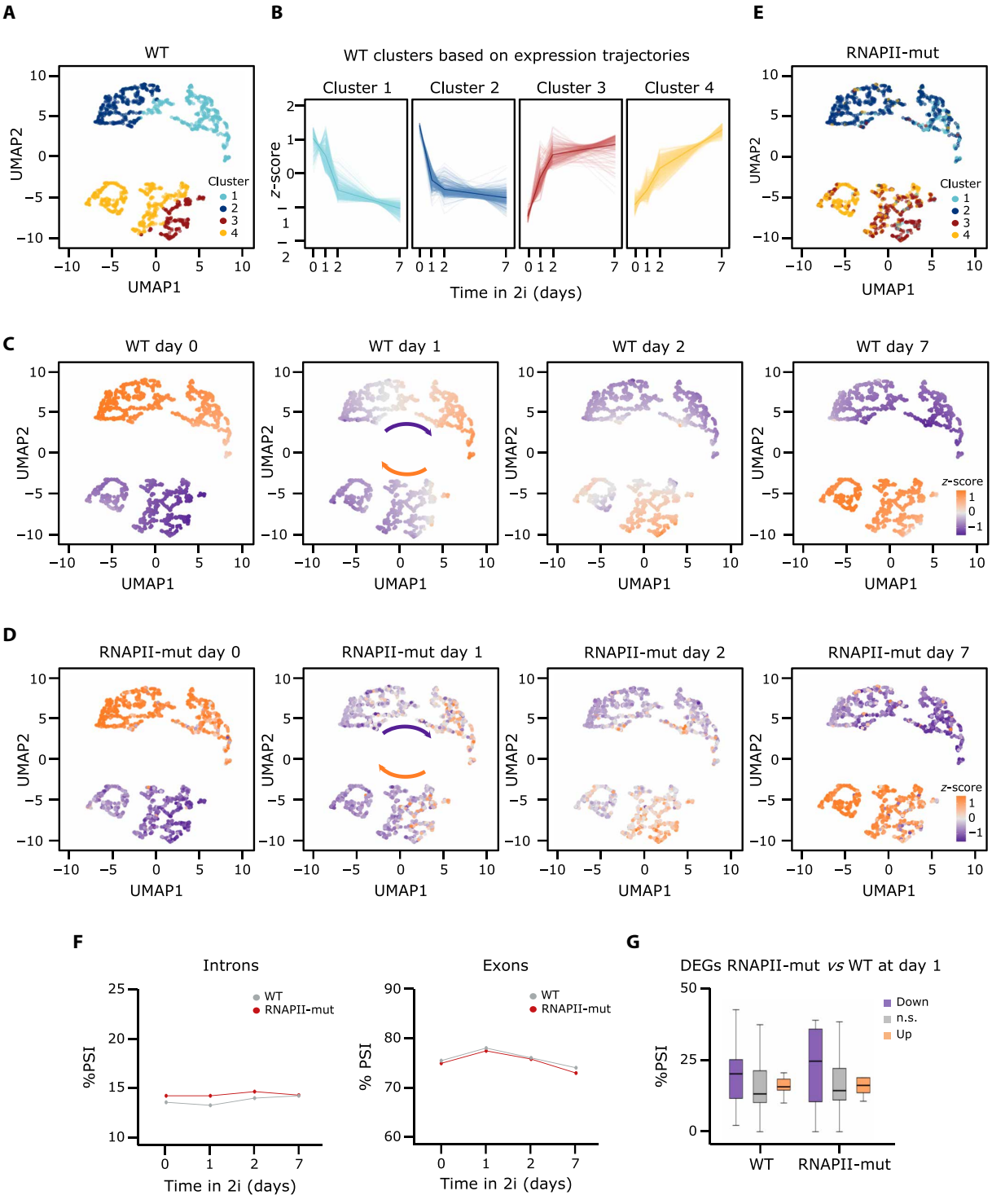

Fig. 6. Slow transcription elongation accelerates the transcriptional switch toward naive pluripotency. (**A**) UMAP analysis representing the similarity of coding genes in terms of their expression levels (*z*-scores) in WT cells, considering the set of genes that are differentially expressed (DEGs) in at least one naive versus pluripotent comparison (d1-d0, d2-d0, or d7-d0) ($n = 1878$ genes). Colors represent gene clusters identified by hierarchical clustering of their expression trajectories across WT dedifferentiation (fig. S5A). (**B**) Trajectories of normalized *z*-score expression levels across WT cells during dedifferentiation (from d0 to d7) of DEGs shown in (A). Cluster 1 (gradual decrease), $n = 517$; cluster 2 (rapid decrease), $n = 460$; cluster 3 (rapid increase), $n = 267$; cluster 4 (gradual increase), $n = 634$. (**C** and **D**) UMAP genes shown in (A) are colored on the basis of normalized *z*-score expression levels at the four time points d0, d1, d2, and d7 in WT cells (C) or RNAPII-mut cells (D). (**E**) UMAP genes shown in (A), colored on the basis of the hierarchical clustering of their expression trajectories across RNAPII-mut cells during dedifferentiation. (**F**) Median PSI values of the indicated AS events in UMAP genes shown in (A) along the primed-to-naive transition. (**G**) PSI distributions of AS events in UMAP genes shown in (A) sorted by their differential expression in the RNAPII-mut versus WT comparison at d1 of dedifferentiation, as indicated. n.s., not significant.

the up-regulation of genes involved in lipid metabolism and catabolic processes (fig. S6B) (*35*, *36*).

As anticipated by the PCAs, projecting gene expression levels along the dedifferentiation course in WT and RNAPII-mut cells revealed that the main differences between cell types were detected at d1, when more genes transitioned to increased or decreased expression in the latter (Fig. 6, C and D, panels for d1). Projection of the gene clusters defined in RNAPII-mut cells on the WT-UMAPs further shows that this observation accounts for changes in gene clusters [i.e., cluster 2 genes (rapid decrease) occupy the space of cluster 1 genes (gradual decrease) and the opposite; cluster 3 genes (rapid increase) occupy the space of cluster 4 genes (gradual increase)] (Fig. 6E). Nevertheless, and in agreement with the similar naive pluripotency stage reached by both cell types, the four gene clusters defined in RNAPII-mut cells comprise functional categories similar to those of the WT ones (fig. S6C). These findings indicate an accelerated reprogramming of gene expression in RNAPII-mut cells.

Although expression changes and AS changes did not correlate (fig. S5E) (*25*), we wondered whether the AS patterns of these UMAP DEGs vary along the dedifferentiation program. For that, we assessed splicing events independently at each time point. DEGs in WT cells showed a tendency toward increasing intron retention over time, reaching a level similar to that in RNAPII-mut cells at the naive stage (Fig. 6F, left). In contrast, exon inclusion levels were parallel in both cell types at all time points (Fig. 6F, right). This behavior indicates that AS patterns are dynamic during primed-to-naive dedifferentiation in WT cells and suggests that, at naive stages, WT cells displayed an AS signature associated with slow transcription elongation, as evidenced by their increased intron retention levels. Supporting this, the genes that respond faster to the dedifferentiation cues in RNAPII-mut cells (the temporarily differential genes at d1) already showed a tendency to gain intron retention events in WT cells, although not as marked as in their mutant counterparts (Fig. 6G). Together, we conclude that slow RNAPII elongation favors a faster transcriptional rewiring toward naive pluripotency.

DISCUSSION

In this study, we examined the effects of slow transcription elongation on DNA replication and stem cell plasticity. We found that decreased transcriptional elongation results in faster replication without causing detectable conflicts between the two processes. This imbalance does not prevent stem cells from effectively transitioning to a naive pluripotent state. Instead, slow-transcribing cells appear predisposed to rewire their transcriptome toward naive pluripotency while maintaining fast replication rates. In addition, we provide evidence that the naive pluripotency state in mESCs and embryos is associated with reduced RNAPII transcription rates. Together, these observations demonstrate that replication and transcription rates do not need to be coordinated to preserve genome function and maintenance and uncover an unexpected link between RNAPII elongation dynamics and cell plasticity.

The R749H mutation in RPB1 lies within the interaction pocket for the general transcription factor TFIIS. Because α-amanitin also inhibits TFIIS-mediated RNA cleavage (*51*), this suggests a shared mechanism of action between α-amanitin and TFIIS in RNAPII elongation (*52*). These insights suggest that the R749H mutation weakens RPB1-TFIIS interactions and thereby hampers pause release. Consistently, the orthologous RNAPII-R741H mutation in *Drosophila* was identified as an α-amanitin–resistant mutant (*53*), reducing the polymerase's ability to read through intrinsic elongation blocks (*27*). Small-molecule inhibitors that disrupt this interaction interface could therefore provide a targeted strategy to modulate transcription elongation while maintaining genome stability, potentially enhancing reprogramming efficiency.

Our work raises several mechanistic questions. First, how does slow transcription elongation lead to faster replication fork progression? Experimental elevation of dNTP levels by exogenous deoxynucleoside supplementation is known to correlate with increased fork speed (*54*). Here, however, the modest increases in dNTP/NTP ratios arise naturally from the naive transition rather than from exogenous manipulation. Because dNTP/NTP levels remain comparable in RNAPII-mut and control cells despite marked differences in transcription and replication rates, nucleotide pool size is unlikely to drive the fast forks in RNAPII-mut cells. As accelerated fork speed can alleviate replication stress in mouse and human ESCs (*55*, *56*), rapid replication may emerge as a compensatory response that minimizes transcription-mediated replicative stress. The absence of elevated transcription-replication encounters in slow-elongating RNAPII cells supports this interpretation. It is also conceivable that reduced RNAPII elongation lowers the buildup of topological stress ahead of transcription complexes (*57*), thereby facilitating replication fork progression. This mechanism may also underlie the heightened sensitivity of RNAPII-mut cells to the increased positive supercoiling produced by Topoisomerase I inhibition. Single-cell measurements of transcription and replication dynamics will be critical for elucidating the mechanistic interplay between these processes. In particular, it will be informative to assess whether the RNAPII-R749H mutation alters the frequency or duration of transcriptional bursting, which could have downstream effects on DNA replication.

Second, the molecular basis of the slow replication forks observed in developing mouse embryos—and recapitulated in vitro during naive pluripotency—remains unclear. Such reduced fork speed may enhance replication fidelity during early development, helping cells accommodate the extensive structural and epigenetic reprogramming characteristic of this stage (*58*, *59*) or facilitate key transcriptional transitions (*38*). However, nucleoside-driven fork acceleration in early embryos appears to proceed without increasing replication errors (*39*), suggesting that fidelity constraints alone do not account for reduced fork velocity. The lack of correlation between elevated dNTP levels and slow forks in naive cells also argues that high nucleotide pools may primarily contribute to genome maintenance, for example, by limiting aberrant deoxyuridine triphosphate (dUTP) or rUTP incorporation (*54*). Whether slow RNAPII elongation similarly contributes to enhanced transcriptional fidelity in early development remains unknown. Notably, (*60*) reported that the overall RNAPII speed increases with age in different organisms and tissues and that these changes in elongation speed were accompanied by changes in splicing. They demonstrated that worms and flies carrying a mutated RNAPII orthologous to the R749H studied here have an increased life span, suggesting that slow RNAPII elongation supports transcriptional accuracy. We therefore propose that RNAPII elongation speed may be actively regulated during the transition through pluripotency, contributing to the acquisition of transcriptional identity at the developmental stage when epiblast and primitive endoderm lineages first diverge (*61*–*63*). Future in vivo studies will be required to test this hypothesis.

Slow RNAPII elongation is also associated with elevated cotranscriptional deposition of N^6-methyladenosine (m^6A) (*64*, *65*), the

most abundant internal mRNA modification in eukaryotes and a key regulator of splicing, RNA stability, and translation (*59*, *66*, *67*). In mESCs, m^6A deposition decreases RNA stability (*68*), which may be related to the observed accelerated silencing of key genes during the dedifferentiation process of RNAPII-mut cells. In addition, the increased intron retention shown by these transcripts might lead to their degradation via nonsense-mediated decay (*43*). Understanding how RNAPII elongation rate, m^6A regulation, and AS converge to fine-tune the balance between naive and primed pluripotency represents an exciting direction for future studies.

MATERIALS AND METHODS

Cell culture and treatments

WT and RNAPII-mut E14 mESCs (kindly provided by J. Cáceres) were grown in Dulbecco's modified Eagle's medium (DMEM) supplemented with 10% fetal bovine serum (FBS) (Gibco), 1x nonessential amino acids, 1 mM sodium pyruvate, 2 mM L-glutamine, 50 μM β-mercaptoethanol, penicillin (100 U/ml)–streptomycin (100 μg/ml) (Invitrogen), and ESGRO mLIF (10^3 U/ml; Millipore) at 37°C and 5% CO_2 on 0.1% gelatin-coated plates. The naive pluripotency state was obtained by adding 1 μM PD0325901 (MEK inhibitor; StemMACS Miltenyi Biotec, #130-103-923) and 3 μM CHIR99021 (GSK3 inhibitor; StemMACS Miltenyi Biotec, #130-103-926) to the same medium and growing the cells for 7 days, changing the media every day and splitting the cells every other day. Cells were routinely tested for mycoplasma contamination.

Aph (Sigma-Aldrich, A0781) treatments were performed at two concentrations (0.1 and 0.5 μM) and incubation times (2.5 and 16 hours), as indicated. CPT (Sigma-Aldrich, C9911) treatments were performed at 5 μM for 2.5 hours.

Cells were synchronized at the G_1-S border by double Thy (Sigma-Aldrich, T1895, SLCG7664) blocking as follows: 2 mM Thy was added to the culture media for 16 hours, and cells were then washed twice with prewarmed phosphate-buffered saline (PBS) and released for 8 hours into a Thy-free medium followed by another 16 hours of incubation with 2 mM Thy.

Cell cycle and cell proliferation analysis

For cell cycle analysis, cells were pulse labeled with 10 μM EdU for 20 min, harvested by trypsinization, fixed with 4% paraformaldehyde (PFA) in PBS for 15 min at room temperature (RT), and permeabilized with 0.25% Triton X-100 for 20 min at RT. EdU incorporation was revealed by Click-iT reaction for 30 min. DNA was stained with 4′,6-diamidino-2-phenylindole (DAPI) in the presence of RNase A/T1 (0.25 mg/ml; Thermo Fisher Scientific, EN0551). Samples were processed in a FACSCanto II cytometer (Becton Dickinson) with FACSDiva v6.1.3 analysis software, and data were analyzed with FlowJo v10 software (Tree Star Inc.).

Cell proliferation was analyzed by CellTrace Violet (Invitrogen, #C34571) according to the manufacturer's instructions. Briefly, harvested cells were labeled in suspension with 5 μM CellTrace Violet dye for 20 min at 37°C. After 2x wash with culture medium with FBS, an equal number of cells were plated to be collected every 12 hours. Samples were fixed and processed as cell cycle analysis samples.

DNA fiber stretching

Exponentially growing cells were sequentially pulse labeled with 50 μM 5-chloro-2′-deoxyuridine (CldU; Sigma-Aldrich, #C6891) and 250 μM 5′-iododeoxyuridine (IdU; Sigma-Aldrich, #I5125) for 20 min each, trypsinized, and collected in cold PBS at a concentration of 2.5×10^5 cells/ml. Two microliters of the cell suspension was lysed by the addition of 10 μl of prewarmed (30°C) spreading buffer [200 mM Tris (pH 7.4), 50 mM EDTA, and 0.5% SDS] on top of a glass slide. After 6-min incubation in a humidity chamber at RT, slides were tilted on a 30° angle to stretch the DNA. Fibers were air dried and fixed with a 3:1 ice-cold methanol:acetic acid solution for 2 min, denaturalized with 2.5 M HCl solution for 30 min at RT, and treated with blocking solution [1% bovine serum albumin (BSA) and 0.1% Triton X-100] for 1 hour. For immunodetection of labeled tracks, samples were incubated with 1:100 anti-CldU (Abcam, Ab6326) and 1:100 anti-IdU (BD Biosciences, 347580) antibodies at 4°C overnight, followed by 1-hour incubation at RT with 1:300 secondary antibodies [anti-rat IgG Alexa Fluor 647 (Thermo Fisher Scientific, 347580) and anti-mouse IgG1 Alexa Fluor 488 (Thermo Fisher Scientific, A21121)]. A third incubation was performed with 1:200 anti-ssDNA (Millipore, MAB3034) and 1:300 anti-mouse IgG2a Alexa Fluor 555 (Thermo Fisher Scientific, A21137) antibodies, simultaneously for 30 min at RT. Following air-drying, slides were mounted with ProLong Glass antiFade medium (Thermo Fisher Scientific, P36984). Images were acquired using a 63X/1.4 oil Plan-Apochromatic objective in an Axiovert200 microscope (Zeiss) and Metamorph 7.10.4.407 software. Analysis of track lengths and origins of replication was performed using Fiji (version 2.14.0). Calculation of fork rate was done on the basis of the conversion factor of 1 μm = 2.59 kb (*69*). Statistical analyses were carried out in Prism v7 (GraphPad Software) using a paired two-tailed *t* test between means, as described in (*70*).

Protein extraction and Western blotting

Whole-protein extracts were obtained with a urea-based solution [8 M urea, 50 mM tris-HCl (pH 8), and 1% CHAPS]. Cell pellets were resuspended in 2 to 3 volumes of extraction buffer and incubated for 30 min at 4°C in agitation. After centrifugation at a maximum speed for 5 min at 4°C, proteins in the soluble fraction were collected and their concentration was assessed by Bradford assay. Biochemical fractionation was performed as described in (*71*).

SDS–polyacrylamide gel electrophoresis (PAGE), protein transfer to a nitrocellulose membrane (Amersham Protran, 0.45 μm), and immunoblotting were performed following standard protocols. Visual acquisition was performed on an Amersham 680-RGB, and band intensities were measured in Fiji. Antibodies used are listed in table S1.

Nucleotide extraction and measurement

An equal number of cells were washed twice with ice-cold tris-buffered saline (TBS) and lysed on ice in TCA-$MgCl_2$ buffer [15% (w/v) trichloroacetic acid and 30 mM $MgCl_2$]. Lysates were scraped, snap frozen in liquid nitrogen, and stored at −80°C until analysis. Nucleotides were extracted, purified, and quantified by high-performance liquid chromatography (HPLC) as described previously (*72*, *73*).

Immunofluorescence and nascent DNA labeling

Cells grown on gelatin-coated glass coverslips were pulse labeled with 10 μM EdU (Merck, 900584) for 20 min for conventional and quantitative image-based cytometry (QIBC) microscopy and 5 min for 3D-SIM. For the 3D-SIM experiments, after EdU pulse, cells were washed with prewarmed PBS and incubated with prewarmed medium for a chase time of 5, 20, 40, and 70 min of chase before fixation. Cells were fixed with 4% PFA (Electron Microscopy Sciences) in PBS

for 15 min and permeabilized with 0.25% Triton X-100 for 20 min at RT. Blocking was carried out with 3% BSA (Sigma-Aldrich) overnight at 4°C for conventional confocal imaging and with MaxBlock (Active Motif) for 30 min at RT for 3D-SIM and QIBC microscopy, before Click-iT reaction to detect EdU and/or primary antibodies incubation.

To the Click-iT reaction cocktail [5 mM $CuSO_4$, 10% tris-HCl (pH 8), and 50 mM sodium ascorbate], 0.5% AZDye488 Azide (Jena Bioscience, CLK1275) was added for conventional microscopy and 0.25% Alexa Fluor 594 Azide (Thermo Fisher Scientific, A10270) for 3D-SIM. Primary antibodies were incubated overnight at 4°C, and secondary antibodies were incubated for 1 hour at RT (table S1). For 3D-SIM imaging, samples were postfixed with 4% PFA for 10 min. Coverslips were counterstained with DAPI (1:1500, Millipore, 5 mg/ml) and mounted with Prolong Glass (Thermo Fisher Scientific, for conventional microscopy), Mowiol (Sigma-Aldrich, 81381, for QIBC), or SlowFade Diamond antifade medium (Thermo Fisher Scientific, for 3D-SIM).

For conventional confocal microscopy image acquisition, an A1R+ confocal microscope (Nikon) with 60x/1.4–numerical aperture (NA) oil objective was used. Nuclei segmentation was automatically performed using the Cellpose Fiji plug-in based on DAPI staining, and nuclear intensity/foci numbers of the different targets were analyzed using custom Fiji scripts.

Proximity ligation assays

PLA was performed using Duolink PLA Technology (Merck), following the manufacturer's instructions. Cells grown in μ-slide 18-well plates (Ibidi, 81816) were permeabilized with 1% Triton X-100 and 4% PFA in 1x PBS for 15 min at RT, washed with PBS, and fixed with 100% ice-cold methanol for 15 min at 4°C before incubating with Blocking Buffer (5% BSA and 10% FBS in 1x PBS) for 1 hour at 37°C in a heated humidity chamber. Mouse anti-PCNA (1:250) and rabbit anti-RNAPIIS2P (1:2000) antibodies were diluted in Blocking Buffer and incubated overnight at 4°C. The Duolink in situ PLA probe anti-rabbit PLUS, Duolink in situ PLA probe anti-mouse MINUS, and Duolink in situ Reagents Far Red were used to perform the PLA reactions according to the manufacturer's guidelines. Last, cells were incubated with DAPI (1:2000, Millipore, 5 mg/ml). Images were acquired with a Zeiss LSM 800 confocal microscope using a 40x oil objective. DAPI-based nuclear segmentation and foci quantification were performed using homemade macros in Fiji, available on request. The workflow included nuclear segmentation using Cellpose (*74*), followed by region of interest (ROI) generation and size-based filtering (retaining areas > 25 px^2). For each segmented and filtered nuclear ROI, the macro counted foci using Find Maxima (prominence = 4000) and measured the mean signal intensity in the relevant channels. All measurements were automatically compiled into an output table for downstream analysis, and more than 833 cells were counted per condition. Statistical analyses were performed in Prism v7 (GraphPad Software) using the nonparametric Mann-Whitney rank sum test.

3D structured illumination microscopy

Super-resolution 3D-SIM imaging was performed on a DeltaVision OMX SR microscope (GE Healthcare), using a 60x/1.5-NA UPLAPO60XOHR oil immersion objective (Olympus). Computational image reconstructions were done using channel-specific optical transfer functions (OTFs) with softWoRx 7.2.0. Before the analysis, postprocessing and quality control of the reconstructed images were carried out using the SIMcheck Fiji plug-in (*75*). Processing consisted of 16-bit conversion and thresholding and quality control median contrast-to-noise (MCN) filtering (*76*). 3D channel registration was performed using Chromagnon 0.92 software (*77*). Quantitative analyses were performed using a custom Fiji macro to calculate the percentage of overlap between DNA being synthesized (EdU) and elongating transcription (RNAPII S2P). Briefly, RNAPII S2P foci centroids were determined and considered as overlapping if colocalizing with an EdU-positive voxel. In parallel, the total number of RNAPII S2P foci per nucleus was quantified, as well as the nuclear volume and DNA content based on DAPI staining. Cells were manually classified as being in the early or mid S phase according to their EdU replication pattern.

Quantitative image-based cytometry

QIBC experiments for detection of γH2AX along the cell cycle were performed on an Olympus ScanR inverted wide-field microscope system based on an IX83 inverted motorized frame (Evident) equipped with hardware autofocus, Semrock DAPI/FITC/Cy3/Cy5 Quad LED filter set, and Lumencor SPECTRA X LED light source and using a UPLXAPO 20x air objective (Olympus) (Fig. 1F) or on a Axio Observer inverted microscope (Zeiss) equipped with an ORCA-Fusion sCMOS camera (C11440-20UP) and Definite Focus, Fast wheel emission filters DAPI/GFP/RFP, using a 40x oil objective (fig. S1G).

For Fig. 1F, images were captured and analyzed using the ScanR acquisition and analysis software 3.2.0 (Evident). Nuclei were segmented, and the cell cycle stage of each cell was determined on the basis of EdU and DAPI mean intensities. The resulting data were visualized using TIBCO Spotfire software (version 12.5.0). For fig. S1G, cells were stained in suspension, and 50,000 were seeded on a μ-Slide 8-well high ibiTreat chamber. Images were captured and analyzed using the ZEN Blue Software (v 3.6) (Zeiss), with *z*-stacks of 30- and 1-μm range, respectively. Orthogonal projections were generated using the same software, and DAPI-based nuclear segmentation and fluorescence intensity quantification were performed using Fiji (ImageJ 1.54p) (*78*) with homemade generated macros, available on request. The workflow included nuclear segmentation using Cellpose (*74*), followed by ROI generation and size-based filtering (retaining areas > 25 px^2). For each segmented and filtered nuclear ROI, the macro measured the raw DAPI signal intensity and the mean signal intensities for EdU and γH2AX. All measurements were automatically compiled into an output table for downstream analysis, and 3000 cells were counted per condition.

Total RNA extraction and sequencing

Cells were resuspended in TRIzol (Thermo Fisher Scientific), and total RNA was subsequently isolated by isopropanol precipitation. RNA samples were treated with DNase using the TURBO DNA-free Kit (Invitrogen) following the manufacturer's instructions.

For total RNA-seq, libraries were prepared using the DNBSEQ eukaryotic strand-specific mRNA kit (Illumina) at BGI Tech Solutions and sequenced on an Illumina DNBSEQ-G400 sequencing platform to produce 150-nt-long paired-end reads at 30M coverage with a Phred quality score of +33.

Pre-mRNA analysis

Transient inhibition of RNAPII Ser^2 phosphorylation with DRB and release was adapted from (*40*) as previously described (*56*). Briefly,

subconfluent cell cultures were incubated in complete medium supplemented with 100 μM DRB for 4 hours. The DRB-containing medium was then washed off, and the fresh medium was added to resume transcription elongation. Total RNA from an equivalent number of cells was isolated every 15 min with the RNeasy kit (Qiagen) following the manufacturer's instructions. One microgram of RNA per time point was treated with TURBO DNA-free (Invitrogen), and reverse transcription reactions were performed with the SuperScript III First Strand Synthesis System (Invitrogen) using random hexamers. Pre-mRNAs at the different time points were quantified by RT-qPCR with primers spanning different exon-intron junctions (*25*). qPCR reactions were performed with a CFX Opus 384 Real-Time PCR System (Bio-Rad) with iTaq Universal SYBR Green Supermix (Bio-Rad). qPCR conditions were empirically tested for each primer pair, and only those showing a slope of $-3.3 \pm 10\%$ and an R^2 value of >0.99 were accepted. All reactions were performed in triplicate in two independent experiments. Quantitative analyses were carried out using the CFX Maestro Software (v2.2). Pre-mRNA values were normalized to the values of the non-DRB–treated sample, which was set to 1. Results are shown as means ± SD.

RNA-seq transcriptomic analyses of protein-coding genes

Sequenced reads were evaluated for quality using FastQC (*79*) and aligned to the mm10 reference genome using STAR (*80*) with standard parameters. BigWig files loaded in the IGV browser (*81*) were generated with the bamCoverage function from deepTools (*82*) using parameters -normalizeUsing CPM and -bs 1. Expression levels in the protein-coding transcriptome were computed with featureCounts (*83*) using the RefSeq annotation (*84*) for the longest transcript variant and normalized by the total read number in each experiment and the gene size.

Differential gene expression analysis between conditions was performed with DESeq2 (*85*). Genes showing adjusted P value < 0.05 and $|\log_2(\text{fold change})| > 0.5$ were considered as significantly differentially expressed (DEGs). GO term enrichment analyses of RNAPII-mut versus WT DEGs at d0 were computed using the enrichGO function from the R clusterProfiler package (*86*) with default parameters and the "BP" (biological processes) ontology category. GO term analysis of UMAP genes clustered according to their trajectories along dedifferentiation was performed using Panther v19.0 (*87*), and the top 10 listed genes, sorted by the smallest false discovery rate (FDR) value, were selected for representation.

The rank-rank hypergeometric overlap (RRHO) test was performed using the ranked list of $\log_2$(fold change) values in the most naive (d7) versus most primed (d0) stages, in WT and RNAPII-mut cells. Heatmap colors represent the $-\log_{10}(P \text{ value})$ after Benjamini-Yekutieli correction of the hypergeometric overlap analysis (*88*).

Hierarchical clustering of DEGs in at least one naive versus primed comparison in WT (d1-d0, d2-d0, or d7-d0) ($n = 1878$ genes) was performed on the basis of their normalized expression levels (z-scores). The UMAP algorithm was applied to these genes to visualize their similarities in terms of expression changes along the primed-to-naive transition using the umap package from R (*89*). For that, we used their normalized expression levels (z-scores) across all time points (d0, d1, d2, and d7). Each UMAP dot represented a gene, which was colored depending on its cluster classification in the hierarchical clustering analyses or its $\log_2$(fold change) value in the RNAPII-mut versus WT differential expression analyses.

Heatmaps were performed using the pheatmap (*90*) package from R. Both violin and boxplots were generated using the ggplot2 package from R (*91*).

AS analysis

AS analysis from total RNA-seq samples was performed using vast-tools v2.5.1 (*92*) with the mm10 mouse VASTDB library (vastdb.mm2.23.06.20.tar.gz). The analyzed event types included "exon," "intron," "alternative 3′ splice site," and "alternative 5′ splice site." We classified "ANN," "S," "C3," "C2," "C1," and "MIC" as exon events. To enhance resolution, we applied the merged function to both replicates under each condition and defined AS events as those with PSI values between 10 and 90%. This strategy precludes statistical testing. Pairwise differential AS analysis was performed using the compare function with parameters --min_dPSI 15 and --min_range 5.

Supplementary Materials

This PDF file includes:

Figs. S1 to S6
Table S1
References

REFERENCES

1. L. Goehring, T. T. Huang, D. J. Smith, Transcription-replication conflicts as a source of genome instability. *Annu. Rev. Genet.* **57**, 157–179 (2023).
2. M. Lalonde, M. Trauner, M. Werner, S. Hamperl, Consequences and resolution of transcription-replication conflicts. *Life (Basel)* **11**, 637 (2021).
3. B. Gómez-González, A. Aguilera, Transcription-mediated replication hindrance: A major driver of genome instability. *Genes Dev.* **33**, 1008–1026 (2019).
4. S. Hamperl, K. A. Cimprich, Conflict resolution in the genome: How transcription and replication make it work. *Cell* **167**, 1455–1467 (2016).
5. K. R. Browning, H. Merrikh, Replication-transcription conflicts: A perpetual war on the chromosome. *Annu. Rev. Biochem.* **93**, 21–46 (2024).
6. Y.-H. Chen, S. Keegan, M. Kahli, P. Tonzi, D. Fenyö, T. T. Huang, D. J. Smith, Transcription shapes DNA replication initiation and termination in human cells. *Nat. Struct. Mol. Biol.* **26**, 67–77 (2019).
7. R. Lombraña, R. Almeida, I. Revuelta, S. Madeira, G. Herranz, N. Saiz, U. Bastolla, M. Gómez, High-resolution analysis of DNA synthesis start sites and nucleosome architecture at efficient mammalian replication origins. *EMBO J.* **32**, 2631–2644 (2013).
8. C. Cayrou, P. Coulombe, A. Vigneron, S. Stanojcic, O. Ganier, I. Peiffer, E. Rivals, A. Puy, S. Laurent-Chabalier, R. Desprat, M. Méchali, Genome-scale analysis of metazoan replication origins reveals their organization in specific but flexible sites defined by conserved features. *Genome Res.* **21**, 1438–1449 (2011).
9. J. Sequeira-Mendes, R. Díaz-Uriarte, A. Apedaile, D. Huntley, N. Brockdorff, M. Gómez, Transcription initiation activity sets replication origin efficiency in mammalian cells. *PLOS Genet.* **5**, e1000446 (2009).
10. Y. Liu, C. Ai, T. Gan, J. Wu, Y. Jiang, X. Liu, R. Lu, N. Gao, Q. Li, X. Ji, J. Hu, Transcription shapes DNA replication initiation to preserve genome integrity. *Genome Biol.* **22**, 176 (2021).
11. R. Lombraña, A. Álvarez, J. M. Fernández-Justel, R. Almeida, C. Poza-Carrión, F. Gomes, A. Calzada, J. M. Requena, M. Gómez, Transcriptionally driven DNA replication program of the human parasite *Leishmania major*. *Cell Rep.* **16**, 1774–1786 (2016).
12. J. Gros, C. Kumar, G. Lynch, T. Yadav, I. Whitehouse, D. Remus, Post-licensing specification of eukaryotic replication origins by facilitated Mcm2-7 sliding along DNA. *Mol. Cell* **60**, 797–807 (2015).
13. S. K. Powell, H. K. MacAlpine, J. A. Prinz, Y. Li, J. A. Belsky, D. M. MacAlpine, Dynamic loading and redistribution of the Mcm2-7 helicase complex through the cell cycle. *EMBO J.* **34**, 531–543 (2015).
14. J. Wang, P. Rojas, J. Mao, M. Mustè Sadurnì, O. Garnier, S. Xiao, M. R. Higgs, P. Garcia, M. Saponaro, Persistence of RNA transcription during DNA replication delays duplication of transcription start sites until G2/M. *Cell Rep.* **34**, 108759 (2021).
15. F. Bruno, C. Coronel-Guisado, C. González-Aguilera, Collisions of RNA polymerases behind the replication fork promote alternative RNA splicing in newly replicated chromatin. *Mol. Cell* **84**, 221–233.e6 (2024).
16. T. K. Fenstermaker, S. Petruk, S. K. Kovermann, H. W. Brock, A. Mazo, RNA polymerase II associates with active genes during DNA replication. *Nature* **620**, 426–433 (2023).
17. T. K. Fenstermaker, S. Petruk, A. Mazo, An emerging paradigm in epigenetic marking: Coordination of transcription and replication. *Transcription* **15**, 22–37 (2024).

18. A. Helmrich, M. Ballarino, E. Nudler, L. Tora, Transcription-replication encounters, consequences and genomic instability. *Nat. Struct. Mol. Biol.* **20**, 412–418 (2013).
19. E. P. C. Rocha, A. Danchin, Essentiality, not expressiveness, drives gene-strand bias in bacteria. *Nat. Genet.* **34**, 377–378 (2003).
20. W.-X. Zheng, C.-S. Luo, Y.-Y. Deng, F.-B. Guo, Essentiality drives the orientation bias of bacterial genes in a continuous manner. *Sci. Rep.* **5**, 16431 (2015).
21. L. F. Liu, J. C. Wang, Supercoiling of the DNA template during transcription. *Proc. Natl. Acad. Sci. U.S.A.* **84**, 7024–7027 (1987).
22. S. French, Consequences of replication fork movement through transcription units in vivo. *Science* **258**, 1362–1365 (1992).
23. E. V. Mirkin, S. M. Mirkin, Mechanisms of transcription-replication collisions in bacteria. *Mol. Cell. Biol.* **25**, 888–895 (2005).
24. S. Hamperl, M. J. Bocek, J. C. Saldivar, T. Swigut, K. A. Cimprich, Transcription-replication conflict orientation modulates R-loop levels and activates distinct DNA damage responses. *Cell* **170**, 774–786.e19 (2017).
25. M. M. Maslon, U. Braunschweig, S. Aitken, A. R. Mann, F. Kilanowski, C. J. Hunter, B. J. Blencowe, A. R. Kornblihtt, I. R. Adams, J. F. Cáceres, A slow transcription rate causes embryonic lethality and perturbs kinetic coupling of neuronal genes. *EMBO J.* **38**, e101244 (2019).
26. J. van den Berg, V. van Batenburg, C. Geisenberger, R. B. Tjeerdsma, A. de Jaime-Soguero, S. P. Acebrón, M. A. T. M. van Vugt, A. van Oudenaarden, Quantifying DNA replication speeds in single cells by scEdU-seq. *Nat. Methods* **21**, 1175–1184 (2024).
27. Y. Chen, D. Chafin, D. H. Price, A. L. Greenleaf, Drosophila RNA polymerase II mutants that affect transcription elongation. *J. Biol. Chem.* **271**, 5993–5999 (1996).
28. F. Ochs, C. Green, A. T. Szczurek, L. Pytowski, S. Kolesnikova, J. Brown, D. W. Gerlich, V. Buckle, L. Schermelleh, K. A. Nasmyth, Sister chromatid cohesion is mediated by individual cohesin complexes. *Science* **383**, 1122–1130 (2024).
29. R. M. Kumar, P. Cahan, A. K. Shalek, R. Satija, A. Jay DaleyKeyser, H. Li, J. Zhang, K. Pardee, D. Gennert, J. J. Trombetta, T. C. Ferrante, A. Regev, G. Q. Daley, J. J. Collins, Deconstructing transcriptional heterogeneity in pluripotent stem cells. *Nature* **516**, 56–61 (2014).
30. P. Cahan, G. Q. Daley, Origins and implications of pluripotent stem cell variability and heterogeneity. *Nat. Rev. Mol. Cell Biol.* **14**, 357–368 (2013).
31. K. M. Loh, B. Lim, A precarious balance: Pluripotency factors as lineage specifiers. *Cell Stem Cell* **8**, 363–369 (2011).
32. A. Martinez Arias, J. M. Brickman, Gene expression heterogeneities in embryonic stem cell populations: Origin and function. *Curr. Opin. Cell Biol.* **23**, 650–656 (2011).
33. J. A. Hackett, M. A. Surani, Regulatory principles of pluripotency: From the ground state up. *Cell Stem Cell* **15**, 416–430 (2014).
34. J. Nichols, A. Smith, Naive and primed pluripotent states. *Cell Stem Cell* **4**, 487–492 (2009).
35. P. Ubieto-Capella, P. Ximénez-Embún, D. Giménez-Llorente, A. Losada, J. Muñoz, J. Méndez, A rewiring of DNA replication mediated by MRE11 exonuclease underlies primed-to-naive cell de-differentiation. *Cell Rep.* **43**, 114024 (2024).
36. A. Martinez-Val, C. J. Lynch, I. Calvo, P. Ximénez-Embún, F. Garcia, E. Zarzuela, M. Serrano, J. Munoz, Dissection of two routes to naïve pluripotency using different kinase inhibitors. *Nat. Commun.* **12**, 1863 (2021).
37. C. J. Lynch, R. Bernad, A. Martínez-Val, M. N. Shahbazi, S. Nóbrega-Pereira, I. Calvo, C. Blanco-Aparicio, C. Tarantino, E. Garreta, L. Richart-Ginés, N. Alcazar, O. Graña-Castro, G. Gómez-Lopez, I. Aksoy, M. Muñoz-Martín, S. Martinez, S. Ortega, S. Prieto, E. Simboeck, A. Camasses, C. Stephan-Otto Attolini, A. F. Fernandez, M. I. Sierra, M. F. Fraga, J. Pastor, D. Fisher, N. Montserrat, P. Savatier, J. Muñoz, M. Zernicka-Goetz, M. Serrano, Global hyperactivation of enhancers stabilizes human and mouse naive pluripotency through inhibition of CDK8/19 mediator kinases. *Nat. Cell Biol.* **22**, 1223–1238 (2020).
38. T. Nakatani, J. Lin, F. Ji, A. Ettinger, J. Pontabry, M. Tokoro, L. Altamirano-Pacheco, J. Fiorentino, E. Mahammadov, Y. Hatano, C. Van Rechem, D. Chakraborty, E. R. Ruiz-Morales, P. Y. Arguello Pascualli, A. Scialdone, K. Yamagata, J. R. Whetstine, R. I. Sadreyev, M.-E. Torres-Padilla, DNA replication fork speed underlies cell fate changes and promotes reprogramming. *Nat. Genet.* **54**, 318–327 (2022).
39. S. Takahashi, H. Kyogoku, T. Hayakawa, H. Miura, A. Oji, Y. Kondo, S. Takebayashi, T. S. Kitajima, I. Hiratani, Embryonic genome instability upon DNA replication timing program emergence. *Nature* **633**, 686–694 (2024).
40. J. Singh, R. A. Padgett, Rates of in situ transcription and splicing in large human genes. *Nat. Struct. Mol. Biol.* **16**, 1128–1133 (2009).
41. T. Saldi, M. A. Cortazar, R. M. Sheridan, D. L. Bentley, Coupling of RNA polymerase II transcription elongation with pre-mRNA splicing. *J. Mol. Biol.* **428**, 2623–2635 (2016).
42. S. Jimeno-González, L. Payán-Bravo, A. M. Muñoz-Cabello, M. Guijo, G. Gutierrez, F. Prado, J. C. Reyes, Defective histone supply causes changes in RNA polymerase II elongation rate and cotranscriptional pre-mRNA splicing. *Proc. Natl. Acad. Sci. U.S.A.* **112**, 14840–14845 (2015).
43. U. Braunschweig, N. L. Barbosa-Morais, Q. Pan, E. N. Nachman, B. Alipanahi, T. Gonatopoulos-Pournatzis, B. Frey, M. Irimia, B. J. Blencowe, Widespread intron retention in mammals functionally tunes transcriptomes. *Genome Res.* **24**, 1774–1786 (2014).
44. G. Dujardin, C. Lafaille, M. de la Mata, L. E. Marasco, M. J. Muñoz, C. Le Jossic-Corcos, L. Corcos, A. R. Kornblihtt, How slow RNA polymerase II elongation favors alternative exon skipping. *Mol. Cell* **54**, 683–690 (2014).
45. N. Fong, H. Kim, Y. Zhou, X. Ji, J. Qiu, T. Saldi, K. Diener, K. Jones, X.-D. Fu, D. L. Bentley, Pre-mRNA splicing is facilitated by an optimal RNA polymerase II elongation rate. *Genes Dev.* **28**, 2663–2676 (2014).
46. J. Y. Ip, D. Schmidt, Q. Pan, A. K. Ramani, A. G. Fraser, D. T. Odom, B. J. Blencowe, Global impact of RNA polymerase II elongation inhibition on alternative splicing regulation. *Genome Res.* **21**, 390–401 (2011).
47. M. de la Mata, C. R. Alonso, S. Kadener, J. P. Fededa, M. Blaustein, F. Pelisch, P. Cramer, D. Bentley, A. R. Kornblihtt, A slow RNA polymerase II affects alternative splicing in vivo. *Mol. Cell* **12**, 525–532 (2003).
48. F. E. Baralle, J. Giudice, Alternative splicing as a regulator of development and tissue identity. *Nat. Rev. Mol. Cell Biol.* **18**, 437–451 (2017).
49. T. Boroviak, R. Loos, P. Lombard, J. Okahara, R. Behr, E. Sasaki, J. Nichols, A. Smith, P. Bertone, Lineage-specific profiling delineates the emergence and progression of naive pluripotency in mammalian embryogenesis. *Dev. Cell* **35**, 366–382 (2015).
50. Q. Deng, D. Ramsköld, B. Reinius, R. Sandberg, Single-cell RNA-seq reveals dynamic, random monoallelic gene expression in mammalian cells. *Science* **343**, 193–196 (2014).
51. M. G. Izban, D. S. Luse, The RNA polymerase II ternary complex cleaves the nascent transcript in a 3′→5′ direction in the presence of elongation factor SII. *Genes Dev.* **6**, 1342–1356 (1992).
52. R. G. Weilbaecher, D. E. Awrey, A. M. Edwards, C. M. Kane, Intrinsic transcript cleavage in yeast RNA polymerase II elongation complexes. *J. Biol. Chem.* **278**, 24189–24199 (2003).
53. Y. Chen, J. Weeks, M. A. Mortin, A. L. Greenleaf, Mapping mutations in genes encoding the two large subunits of *Drosophila* RNA polymerase II defines domains essential for basic transcription functions and for proper expression of developmental genes. *Mol. Cell. Biol.* **13**, 4214–4222 (1993).
54. P. Pandey, K. Kurashima, G. Bylund, E. Johansson, T. Tsubouchi, A. Chabes, Decoding nucleoside supplementation: How thymidine outperforms ribonucleosides in accelerating mammalian replication forks. *Nucleic Acids Res.* **53**, gkaf1035 (2025).
55. J. A. Halliwell, T. J. R. Frith, O. Laing, C. J. Price, O. J. Bower, D. Stavish, P. J. Gokhale, Z. Hewitt, S. F. El-Khamisy, I. Barbaric, P. W. Andrews, Nucleosides rescue replication-mediated genome instability of human pluripotent stem cells. *Stem Cell Rep.* **14**, 1009–1017 (2020).
56. R. Almeida, J. M. Fernández-Justel, C. Santa-María, J.-C. Cadoret, L. Cano-Aroca, R. Lombraña, G. Herranz, A. Agresti, M. Gómez, Chromatin conformation regulates the coordination between DNA replication and transcription. *Nat. Commun.* **9**, 1590 (2018).
57. S. Tripathi, S. Brahmachari, J. N. Onuchic, H. Levine, DNA supercoiling-mediated collective behavior of co-transcribing RNA polymerases. *Nucleic Acids Res.* **50**, 1269–1279 (2022).
58. M. Pal, T. Schauer, A. Burton, T. Nakatani, F. Pecori, A. Hernández-Giménez, I. Nadelson, M. A. Marti-Renom, M.-E. Torres-Padilla, The establishment of nuclear organization in mouse embryos is orchestrated by multiple epigenetic pathways. *Cell* **188**, 3583–3602.e21 (2025).
59. Y. Ke, Y. Xu, X. Chen, S. Feng, Z. Liu, Y. Sun, X. Yao, F. Li, W. Zhu, L. Gao, H. Chen, Z. Du, W. Xie, X. Xu, X. Huang, J. Liu, 3D chromatin structures of mature gametes and structural reprogramming during mammalian embryogenesis. *Cell* **170**, 367–381.e20 (2017).
60. C. Debès, A. Papadakis, S. Grönke, Ö. Karalay, L. S. Tain, A. Mizi, S. Nakamura, O. Hahn, C. Weigelt, N. Josipovic, A. Zirkel, I. Brusius, K. Sofiadis, M. Lamprousi, Y.-X. Lu, W. Huang, R. Esmaillie, T. Kubacki, M. R. Späth, B. Schermer, T. Benzing, R.-U. Müller, A. Antebi, L. Partridge, A. Papantonis, A. Beyer, Ageing-associated changes in transcriptional elongation influence longevity. *Nature* **616**, 814–821 (2023).
61. C. Bassalert, L. Valverde-Estrella, C. Chazaud, "Chapter five—Primitive endoderm differentiation: From specification to epithelialization" in *Current Topics in Developmental Biology*, vol. 128 of *Cell Fate in Mammalian Development*, B. Plusa, A.-K. Hadjantonakis, Eds. (Academic Press, 2018), pp. 81–104.
62. T. Boroviak, J. Nichols, The birth of embryonic pluripotency. *Philos. Trans. R. Soc. London Ser. B Biol. Sci.* **369**, 20130541 (2014).
63. Y. Ohnishi, W. Huber, A. Tsumura, M. Kang, P. Xenopoulos, K. Kurimoto, A. K. Oleś, M. J. Araúzo-Bravo, M. Saitou, A.-K. Hadjantonakis, T. Hiiragi, Cell-to-cell expression variability followed by signal reinforcement progressively segregates early mouse lineages. *Nat. Cell Biol.* **16**, 27–37 (2014).
64. A. Gallego, J. M. Fernández-Justel, S. Martín-Vírgala, M. M. Maslon, M. Gómez, Slow RNAPII transcription elongation rate, low levels of RNAPII pausing, and elevated histone H1 content at promoters associate with higher m6A deposition on nascent mRNAs. *Genes* **13**, 1652 (2022).
65. B. Slobodin, R. Han, V. Calderone, J. A. F. O. Vrielink, F. Loayza-Puch, R. Elkon, R. Agami, Transcription Impacts the efficiency of mRNA translation via co-transcriptional N6-adenosine methylation. *Cell* **169**, 326–337.e12 (2017).
66. A. Louloupi, E. Ntini, T. Conrad, U. A. V. Ørom, Transient N-6-methyladenosine transcriptome sequencing reveals a regulatory role of m6A in splicing efficiency. *Cell Rep.* **23**, 3429–3437 (2018).

67. I. Barbieri, K. Tzelepis, L. Pandolfini, J. Shi, G. Millán-Zambrano, S. C. Robson, D. Aspris, V. Migliori, A. J. Bannister, N. Han, E. De Braekeleer, H. Ponstingl, A. Hendrick, C. R. Vakoc, G. S. Vassiliou, T. Kouzarides, Promoter-bound METTL3 maintains myeloid leukaemia by m6A-dependent translation control. *Nature* **552**, 126–131 (2017).
68. J. Liu, X. Dou, C. Chen, C. Chen, C. Liu, M. M. Xu, S. Zhao, B. Shen, Y. Gao, D. Han, C. He, N^6-methyladenosine of chromosome-associated regulatory RNA regulates chromatin state and transcription. *Science* **367**, 580–586 (2020).
69. D. A. Jackson, A. Pombo, Replicon clusters are stable units of chromosome structure: Evidence that nuclear organization contributes to the efficient activation and propagation of S phase in human cells. *J. Cell Biol.* **140**, 1285–1295 (1998).
70. S. J. Lord, K. B. Velle, R. D. Mullins, L. K. Fritz-Laylin, SuperPlots: Communicating reproducibility and variability in cell biology. *J. Cell Biol.* **219**, e202001064 (2020).
71. J. Méndez, B. Stillman, Chromatin association of human origin recognition complex, Cdc6, and minichromosome maintenance proteins during the cell cycle: Assembly of prereplication complexes in late mitosis. *Mol. Cell. Biol.* **20**, 8602–8612 (2000).
72. B. Das, P. Mishra, P. Pandey, S. Sharma, A. Chabes, dNTP concentrations do not increase in mammalian cells in response to DNA damage. *Cell Metab.* **34**, 1895–1896 (2022).
73. S. Jia, L. Marjavaara, R. Buckland, S. Sharma, A. Chabes, "Determination of deoxyribonucleoside triphosphate concentrations in yeast cells by strong anion-exchange high-performance liquid chromatography coupled with ultraviolet detection" in *DNA Replication: Methods and Protocols*, S. Vengrova, J. Dalgaard, Eds. (Springer, 2015), pp. 113–121.
74. C. Stringer, T. Wang, M. Michaelos, M. Pachitariu, Cellpose: A generalist algorithm for cellular segmentation. *Nat. Methods* **18**, 100–106 (2021).
75. G. Ball, J. Demmerle, R. Kaufmann, I. Davis, I. M. Dobbie, L. Schermelleh, SIMcheck: A toolbox for successful super-resolution structured illumination microscopy. *Sci. Rep.* **5**, 15915 (2015).
76. L. Rodermund, H. Coker, R. Oldenkamp, G. Wei, J. Bowness, B. Rajkumar, T. Nesterova, D. M. Susano Pinto, L. Schermelleh, N. Brockdorff, Time-resolved structured illumination microscopy reveals key principles of Xist RNA spreading. *Science* **372**, eabe7500 (2021).
77. A. Matsuda, L. Schermelleh, Y. Hirano, T. Haraguchi, Y. Hiraoka, Accurate and fiducial-marker-free correction for three-dimensional chromatic shift in biological fluorescence microscopy. *Sci. Rep.* **8**, 7583 (2018).
78. J. Schindelin, I. Arganda-Carreras, E. Frise, V. Kaynig, M. Longair, T. Pietzsch, S. Preibisch, C. Rueden, S. Saalfeld, B. Schmid, J.-Y. Tinevez, D. J. White, V. Hartenstein, K. Eliceiri, P. Tomancak, A. Cardona, Fiji: An open-source platform for biological-image analysis. *Nat. Methods* **9**, 676–682 (2012).
79. S. Andrews, FastQC: A Quality Control Tool for High Throughput Sequence (2010); http://bioinformatics.babraham.ac.uk/projects/fastqc/.
80. A. Dobin, C. A. Davis, F. Schlesinger, J. Drenkow, C. Zaleski, S. Jha, P. Batut, M. Chaisson, T. R. Gingeras, STAR: Ultrafast universal RNA-seq aligner. *Bioinformatics* **29**, 15–21 (2013).
81. J. T. Robinson, H. Thorvaldsdóttir, W. Winckler, M. Guttman, E. S. Lander, G. Getz, J. P. Mesirov, Integrative genomics viewer. *Nat. Biotechnol.* **29**, 24–26 (2011).
82. F. Ramírez, D. P. Ryan, B. Grüning, V. Bhardwaj, F. Kilpert, A. S. Richter, S. Heyne, F. Dündar, T. Manke, deepTools2: A next generation web server for deep-sequencing data analysis. *Nucleic Acids Res.* **44**, W160–W165 (2016).
83. Y. Liao, G. K. Smyth, W. Shi, featureCounts: An efficient general purpose program for assigning sequence reads to genomic features. *Bioinformatics* **30**, 923–930 (2014).
84. N. A. O'Leary, M. W. Wright, J. R. Brister, S. Ciufo, D. Haddad, R. McVeigh, B. Rajput, B. Robbertse, B. Smith-White, D. Ako-Adjei, A. Astashyn, A. Badretdin, Y. Bao, O. Blinkova, V. Brover, V. Chetvernin, J. Choi, E. Cox, O. Ermolaeva, C. M. Farrell, T. Goldfarb, T. Gupta, D. Haft, E. Hatcher, W. Hlavina, V. S. Joardar, V. K. Kodali, W. Li, D. Maglott, P. Masterson, K. M. McGarvey, M. R. Murphy, K. O'Neill, S. Pujar, S. H. Rangwala, D. Rausch, L. D. Riddick, C. Schoch, A. Shkeda, S. S. Storz, H. Sun, F. Thibaud-Nissen, I. Tolstoy, R. E. Tully, A. R. Vatsan, C. Wallin, D. Webb, W. Wu, M. J. Landrum, A. Kimchi, T. Tatusova, M. DiCuccio, P. Kitts, T. D. Murphy, K. D. Pruitt, Reference sequence (RefSeq) database at NCBI: Current status, taxonomic expansion, and functional annotation. *Nucleic Acids Res.* **44**, D733–D745 (2016).
85. M. I. Love, W. Huber, S. Anders, Moderated estimation of fold change and dispersion for RNA-seq data with DESeq2. *Genome Biol.* **15**, 550 (2014).
86. G. Yu, L.-G. Wang, Y. Han, Q.-Y. He, clusterProfiler: An R package for comparing biological themes among gene clusters. *OMICS J. Integr. Biol.* **16**, 284–287 (2012).
87. H. Mi, A. Muruganujan, D. Ebert, X. Huang, P. D. Thomas, PANTHER version 14: More genomes, a new PANTHER GO-slim and improvements in enrichment analysis tools. *Nucleic Acids Res.* **47**, D419–D426 (2019).
88. S. B. Plaisier, R. Taschereau, J. A. Wong, T. G. Graeber, Rank–rank hypergeometric overlap: Identification of statistically significant overlap between gene-expression signatures. *Nucleic Acids Res.* **38**, e169 (2010).
89. T. Konopka, umap: Uniform manifold approximation and projection. R package version 0.2.11.0 (2025); https://github.com/tkonopka/umap.
90. R. Kolde, pheatmap: Pretty Heatmaps. R package version 1.0.12 (2019); https://CRAN.R-project.org/package=pheatmap.
91. H. Wickham, *Ggplot2*, Use R! (Springer International Publishing, 2016).
92. J. Tapial, K. C. H. Ha, T. Sterne-Weiler, A. Gohr, U. Braunschweig, A. Hermoso-Pulido, M. Quesnel-Vallières, J. Permanyer, R. Sodaei, Y. Marquez, L. Cozzuto, X. Wang, M. Gómez-Velázquez, T. Rayon, M. Manzanares, J. Ponomarenko, B. J. Blencowe, M. Irimia, An atlas of alternative splicing profiles and functional associations reveals new regulatory programs and genes that simultaneously express multiple major isoforms. *Genome Res.* **27**, 1759–1768 (2017).
93. S. Martín-Vírgala, J. Segura, A. Gallego, R. Tong, S. Tur-Gracia, J. R. Rodriguez-Aguilera, B. Das, J. Isoler-Alcaraz, C. Galleo-Carcia, S. Shinde, M. M. Maslon, A. Chabes, L. Schermelle, M. Gomez, Slow-RNAPII-RNAseq, Zenodo (2026); https://doi.org/10.5281/zenodo.19066623.
94. T. Barrett, S. E. Wilhite, P. Ledoux, C. Evangelista, I. F. Kim, M. Tomashevsky, K. A. Marshall, K. H. Phillippy, P. M. Sherman, M. Holko, A. Yefanov, H. Lee, N. Zhang, C. L. Robertson, N. Serova, S. Davis, A. Soboleva, NCBI GEO: Archive for functional genomics data sets—Update. *Nucleic Acids Res.* **41**, D991–D995 (2013).
95. S. Alvarez, M. Díaz, J. Flach, S. Rodriguez-Acebes, A. J. López-Contreras, D. Martínez, M. Cañamero, O. Fernández-Capetillo, J. Isern, E. Passegué, J. Méndez, Replication stress caused by low MCM expression limits fetal erythropoiesis and hematopoietic stem cell functionality. *Nat. Commun.* **6**, 8548 (2015).

Acknowledgments: We thank J. Cáceres for the gift of RNAPII-mut mESC cells. We are also grateful to T. Nesterova and N. Brockdorff for support during S.M.-V.'s stay at the Biochemistry Department, University of Oxford. We further acknowledge technical support from the Micron Oxford Bioimaging Facility and the Advanced Light Microscopy Facility (SMOA) at the CBM. **Funding:** This work was supported by grant PID2022-141380NB-I00 funded by MICIU/AEI/10.13039/501100011033 and ERDF/EU (MG), grant "Excelencia Severo Ochoa" CEX2021-001154-S funded by MICIU/AEI/10.13039/501100011033 (M.G.), CSIC 2023AEP011 (M.G.), grant FPU18/04794 funded by the MICIU/AEI/10.13039/501100011033 and FSE (S.M.-V.), EMBO short-term fellowship 9872 (S.M.-V.), grant FJC2021-047498-I funded by MCIN/AEI/10.13039/501100011033 and European Union NextGenerationEU/PRTR (J.S.), postdoctoral grant POSTD258466SEGU funded by the Scientific Foundation of the Spanish Association Against Cancer (J.S.), RepliFate Doctoral Network [HORIZON-MSCA-2021-DN-01-01 Project 101072903] (R.T.), grant FPU20/02167 funded by MICIU/AEI/10.13039/501100011033 and FSE (S.T.-G.), postdoctoral grant "Excelencia Severo Ochoa" CEX2021-001154-S funded by MICIU/AEI/10.13039/501100011033 (J.R.R.-A.), grant PRE2020-095071 funded by MICIU/AEI/10.13039/501100011033 and FSE (J.I.-A.), Swedish Research Council [2022-00675] and Swedish Cancer Society [22 2377 Pj] (A.C.), SSMF postdoctoral grant [PG-22-0342] (B.D.), National Science Centre (NCN, Poland) research grant [Sonata Bis Grant UMO-2020/38/E/NZ1/00070] (M.M.M. and S.S.), and Polish National Agency for Academic Exchange [BPN/PPO/2021/1/00031/U/0000] (M.M.M. and S.S.). **Author contributions:** Conceptualization: M.G. Investigation: S.M.-V., J.S., R.T., S.T.-G., J.R.R.-A., B.D., J.I.-A., C.G.-G., S.S., and M.M.M. Visualization: S.M.-V., L.S., and M.G. Formal analysis: S.M.-V., J.S., and A.G. Supervision: M.M.M., A.C., L.S., and M.G. Writing—original draft: S.M.-V. and M.G. Writing—review and editing: J.S., A.G., M.M.M., A.C., L.S., and M.G. **Competing interests:** The authors declare that they have no competing interests. **Data, code, and materials availability:** All data and code needed to evaluate and reproduce the results in the paper are present in the paper and/or the Supplementary Materials. No new materials were generated for this work. All scripts used are publicly available at the GitHub repository, which is only used as an additional resource: https://github.com/aliciagallego/Slow-RNAPII-RNAseq and archived at Zenodo (*93*). Total RNA-seq data generated and analyzed in this work have been deposited in the NCBI Gene Expression Omnibus database (*94*) under the accession number GSE293593 (https://ncbi.nlm.nih.gov/geo/query/acc.cgi?acc=GSE293593). The following GEO and ArrayExpress datasets were analyzed in this study: RNA-seq from WT mESCs in serum/LIF and serum/LIF and 2i [GSE112208 (https://ncbi.nlm.nih.gov/geo/query/acc.cgi?acc=GSE112208) and GSE254126 (https://ncbi.nlm.nih.gov/geo/query/acc.cgi?acc=GSE254126)], RNA-seq from mouse embryos at E3.5 and E4.5 stages (E-MTAB-2958; https://ebi.ac.uk/biostudies/arrayexpress/studies/E-MTAB-2958), single-cell RNA-seq from mid and late blastocyst stages (GSE45719; https://ncbi.nlm.nih.gov/geo/query/acc.cgi?acc=GSE45719), and RNA-seq from WT and RNAPII-mut (slow/slow) mESCs (GSE127741; https://ncbi.nlm.nih.gov/geo/query/acc.cgi?acc=GSE127741).

Submitted 8 June 2025
Accepted 20 March 2026
Published 24 April 2026
10.1126/sciadv.adz6211